The viscous-brittle transition in flowing crystal-bearing volcanic dome lavas

Fabian B. Wadsworth [a,*], Jérémie Vasseur [b], Michael J. Heap [c,d], Jackie E. Kendrick [b], Claire E. Harnett [e], Annabelle Foster [a], Daniel Weller [b], Bettina Scheu [b], Anthony Lamur [b], Luiz Pereira [b], Donald B. Dingwell [b], Yan Lavallée [b]

[a] Earth Sciences, Durham University, Durham DH1 3LE, UK
[b] Department of Earth and Environmental Science, Ludwig-Maximilians-Universität München, Theresienstr. 41, 80333, München, Germany
[c] Université de Strasbourg, CNRS, Institut Terre et Environnement de Strasbourg, UMR 7063, 5 rue René Descartes, Strasbourg F-67084, France
[d] Institut Universitaire de France (IUF), Paris, France
[e] School of Earth Sciences, University College Dublin, Dublin, Ireland

ABSTRACT

The ascent and advance of volcanic dome lava is non-linear and viscoelastic. There exists a mismatch between current theoretical approaches to dome lava rheology, which are based on rheological laws for viscous suspensions, and empirical experimental approaches to convolved viscous-brittle deformation, which show mixed evidence for simultaneous lava flow and fracturing. The missing requirement is a unified framework for understanding the transition between micro-mechanical flow mechanisms that are dominantly viscous, and those that include micro-cracking in multiphase suspensions such as magmas. Here, we use high-temperature compression rheology with sample-scale acoustic emission analysis to constrain the conditions under which crystal-rich volcanic dome lava can flow by mixed viscous and brittle fracturing processes at small scales, leading to 'crackling' acoustic signals, even at moderate shear stresses extant in nature. Using multi-directional permeability measurements on large 60 mm diameter quenched samples of natural magmas, we show that this micro-cracking flow mechanism leads to permeability anisotropy, localizing outgassing into pathways that are off-axis relative to the direction of flow. Finally, we use a scaling approach and a database of published observations from real eruptions to upscale our findings, and show that bulk, apparently ductile flow of low-porosity dome magma is likely to involve a local mixed-mode of micro-cracking and viscous flow during the shallowest portions of ascent and during emplacement on the Earth's surface. The micro-cracking involved in lava advance divorces real crystal-bearing lava emplacement from most current rheology models based on a purely viscous micro-mechanism and shows that a revised solution for the rheology of mixed brittle-viscous flow is required. By re-examining published numerical models for dome emplacement, we demonstrate that the viscous-brittle transition can be intercepted in spatially heterogeneous zones within the dome core.

1. Introduction

The growth and flow of lava domes is non-linear and complex (Melnik and Sparks, 1999; Calder et al., 2015). Lava domes – mounds of high viscosity degassed magma accumulated in a volcanic vent region – are thought to act as low permeability plugs, capping the volcanic conduit and preventing pressurized volcanic gas from escaping, potentially leading to an overpressure-driven Vulcanian eruption (Sparks, 1997; Stix et al., 1997; Voight and Elsworth, 2000; Lavallée et al., 2013;

Kendrick et al., 2013; Ashwell et al., 2015; Heap et al., 2019). These processes can lead to dome collapse producing hazardous block-and-ash flows (Rose, 1973; Voight and Elsworth, 2000). The propensity both for dome lava to accommodate underlying sustained volcanic gas overpressure, and for domes to produce unstable steep sides, are likely to be controlled by their continuum rheology. Despite substantial advances in the understanding of multiphase magma rheology (Caricchi et al., 2007; Lavallée et al., 2007; Deubelbeiss et al., 2011; Avard and Whittington, 2012; Pistone et al., 2012, 2015; Cordonnier et al., 2012a; Mader et al.,

---

* Corresponding author.
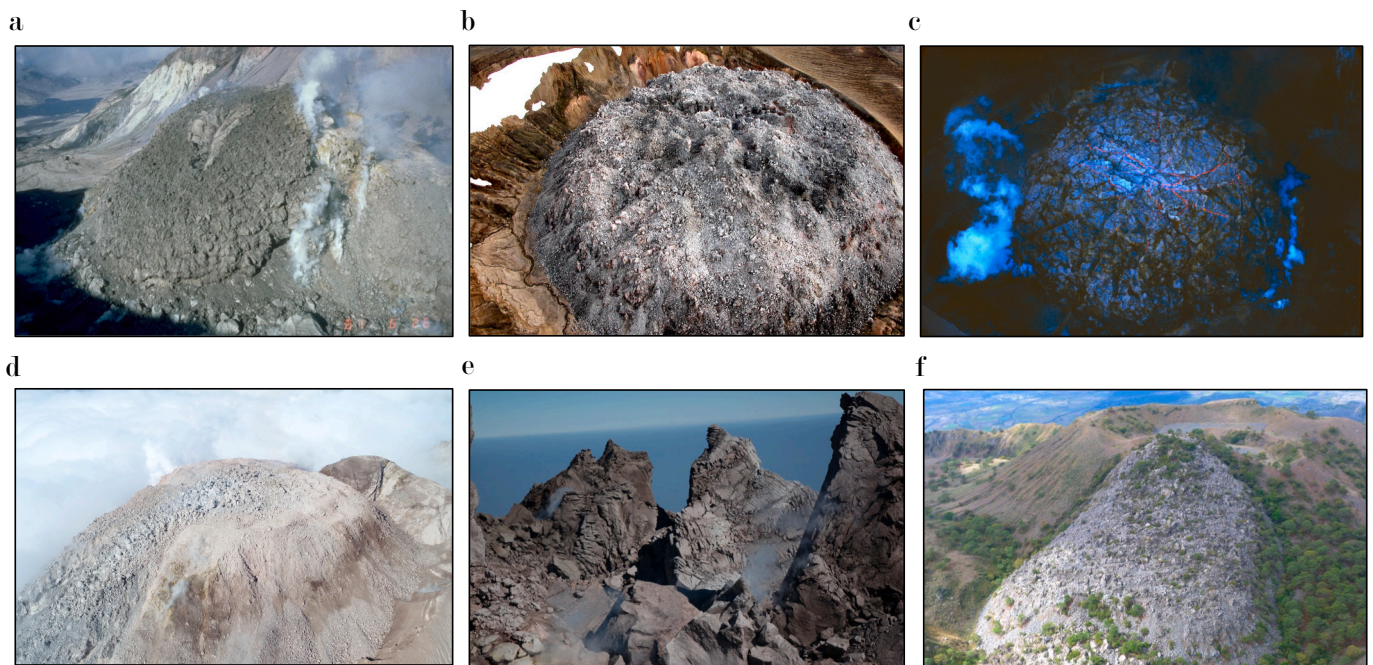*E-mail address:* fabian.wadsworth@gmail.com (F.B. Wadsworth).

Fig. 1. Lava dome morphologies, rubbly surfaces, and interiors. (a) An oblique view of the 1980–86 dome complex at Mt. St Helens volcano (U.S.A.). (b) The 1912 Novarupta lava dome (U.S.A.; photograph taken in July 1987). (c) A top-down view of the 1980 lava dome at Mt. St Helens (USA). (d) Lava extruding from the lava dome to the left of the image at Santiaguito volcano (Guatemala) from February 2019. (e) The interior region of the 1991–95 Mt. Unzen lava dome. (f) The lava dome at Ceboruco volcano (Mexico) with rubbly top and talus-covered slopes. The photograph shown in (a) was taken by Dan Dzurisin (public domain), that in (b) by Cyrus Read (courtesy of USGS and the Alaskan Volcano Observatory) and the photo in (c) appears in Heap et al. (2016) (Copyright© 1980 Gary Braasch Photography; photograph used here with permission from Gary Braasch). The photo in (d) appears in Zorn et al. (2020). The photos in (e-f) are from Yan Lavallée. Scales are not given in many of these images because of perspective, but each dome is of the order of tens of meters across (see original publications for more information). The field of view in (e) is ~80 m.

2013; Kendrick et al., 2013; Coats et al., 2018; Vasseur et al., 2023, 2024), the question of how the complex flow of dome lavas in the laboratory upscales to conditions of emplacement remains unanswered. Central outstanding issues surround (1) the way that the stresses driving flow are partitioned between phases and (2) the propensity for micro-cracking behaviour arising from magmatic liquid viscoelasticity, crystal-crystal force chains at high crystallinity, or both.

Dome lavas are commonly crystal-rich, variably porous, and internally fractured (Calder et al., 2015). Experimental and numerical evidence shows that a high proportion of crystals in magma can act to locally concentrate shear stresses in hot dome lavas during flow (Deubelbeiss et al., 2011; Cordonnier et al., 2012a; Vasseur et al., 2023), and can substantially reduce the bulk stresses required for fracturing compared with the stresses required to induce viscoelastic fracture in crystal-free magmatic liquids (Webb and Dingwell, 1990; Cordonnier et al., 2012b, 2012a; Coats et al., 2018; Wadsworth et al., 2018; Vasseur et al., 2023). The propensity for dome magmas to fracture, rather than flow in a purely viscous manner, has been documented in laboratory experiments designed to measure the viscosity of such multiphase materials, where (1) deformation at high temperature has resulted in acoustic emissions indicative of micro-fracturing (Lavallée et al., 2008; Tuffen et al., 2008; Smith et al., 2011) and (2) the post-experimental samples exhibit clear fracture textures (Lavallée et al., 2007, 2013; Cordonnier et al., 2012a; Kendrick et al., 2013, 2017; Coats et al., 2018). Such observations raise the question is the dominant dome emplacement mechanism viscous, or a mixed viscous-brittle mechanism?. For purposes of simplification, models for the ascent and eruption of crystal-bearing magmas such as dome lavas generally presume the former case, typically employing a suspension viscosity to relate the stress sustained during flow to the resultant rates of flow (Melnik and Sparks, 1999; Holland et al., 2011; Mueller et al., 2011; Zorn et al., 2020; Adam et al., 2024). In most cases, this is necessary because it is not feasible to explicitly numerically solve for micro-fracturing processes at the scale of

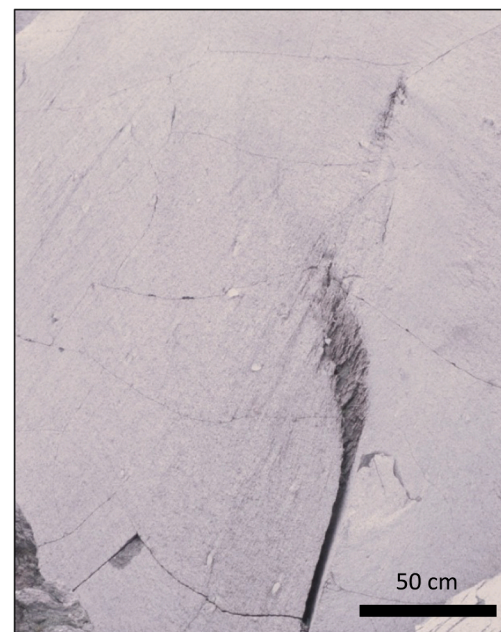**Fig. 2.** A fracture internal to a lava spine erupted during the 1991–95 eruption sequence of Mt. Unzen, Japan (Goto, 1999; Lavallée and Kendrick, 2022) showing purely brittle strain localization at the bottom of the image feathering upward into viscous-brittle distributed damage.

crystals over domains as large as conduits or domes and yet careful post-eruption examination demonstrates crystal-scale fracturing is present (see Lavallée et al., 2022 for field evidence for this crystal-scale fracturing). Therefore, a reasonable experimental goal might be to first define the conditions under which lavas will internally fracture, and then second, to attribute a different continuum rheology to micro-structurally damaged lava versus non-damaged lava. Here, a central aim is to better describe the physical regimes in which a purely viscous and a purely brittle response to an imposed stress may be predicted, placing model approaches on a firmer footing in terms of the assumed rheology.

Actively advancing lava domes exhibit rubbly surface morphologies in nature (Fig. 1; Heap et al., 2016; Varley et al., 2019; Zorn et al., 2019, 2020), and surface break-up during emplacement is common. This break-up can be thermally controlled such that the rubbly brittle cara-pace forms by the break-up of colder lava crusts. However, where areas of the internal structure of lava domes are exposed after an eruption, there is textural evidence for internal strain localisation in the form of fractures on a variety of scales within the lava (Fig. 2), which are thought to have formed via a viscoelastic response to flow-induced stresses, rather than during cooling (Goto, 1999; Lavallée et al., 2013; Kendrick et al., 2016; Goto et al., 2020; Andrews et al., 2021). Multiscale fracturing cannot be generated by purely viscous mechanisms and provide direct observational evidence that a mixed viscous-brittle visco-elastic rheology description may be required.

A detailed understanding of how dome lavas advance – purely viscously or with a component of distributed or localized cracking – has important consequences for the evolution of porosity and permeability. If dome lavas are undergoing pervasive fracturing on a small scale, or fracturing on an intermediate-to-large scale, this could manifest itself in a substantial permeability change (Lavallée et al., 2013, 2022; Farquharson et al., 2016; Kendrick et al., 2021). Because dome lavas generally flow only short distances from the vent, and commonly occlude the vent area of active dome-forming volcanoes, their permeability magnitude and anisotropy may be key to understanding how pressurized volatile fluids outgas from the underlying conduit. By studying suites of dome materials from dome-forming volcanoes, Farquharson et al. (2016) constrained up to ~ 2.5 orders of magnitude of difference between the permeabilities in two mutually perpendicular directions. While permeability in a given direction has been shown experimentally to change with progressive shear strain and to develop anisotropy (Kendrick et al., 2013; Ashwell et al., 2015), it remains unclear under what range of deformation conditions such anisotropy is prevalent. This knowledge-gap exists in part because it is experimentally challenging to determine the permeability in multiple directions on a single experimental sample after a strain has been induced at high temperature and after cooling.

Here, we deformed especially large (up to 60 mm diameter) cylindrical samples of crystal-rich andesitic dome lava from Volcán de Colima (Mexico) in high-temperature experimental deformation tests in order to: (1) measure the strain rate as a result of applied stress; (2) record acoustic emissions indicative of fracturing; and (3) generate deformed samples on which post-test permeability measurements may be made in three orthogonal directions. We supplement these main goals with additional experiments to constrain the rheology of the same dome lava specifically in the absence of cracking. Our goal is to test the hypothesis that at applied stresses typical of dome emplacement, dome lavas can appear to flow in a ductile manner, and yet flow can be accommodated in-part by micro-cracking. We use our results along with compiled published experimental and numerical data to underpin a simple scaling for the brittle threshold in multiphase dome lavas and to infer whether dome lavas emplace dominantly in the viscous or brittle field.

2. Existing challenges and opportunities

Experimental work has previously explicitly acknowledged that the

deformation of dome lavas is variably accommodated by viscous-brittle cracking (Lavallée et al., 2007, 2008, 2013; Tuffen et al., 2008; Smith et al., 2011; Pistone et al., 2015, 2012; Cordonnier et al., 2012a; Kendrick et al., 2013, 2017; Coats et al., 2018; Wadsworth et al., 2018; Hornby et al., 2019; Andrews et al., 2021; Vasseur et al., 2023). Similarly, fracturing during dome advance has been identified in the field or inferred during volcano monitoring efforts (Matthews et al., 1997; Goto, 1999; Watts et al., 2002; Neuberg et al., 2006; Sherrod et al., 2008; Holland et al., 2011; Thomas and Neuberg, 2012; Goto et al., 2020; Lavallée et al., 2022). At Lascar volcano (Chile), arcuate dome-hosted fractures opened up in concentric patterns during dome subsidence (Matthews et al., 1997). Fracture-hosted *syn*-emplacement outgassing through piles of dome lava has been inferred at Soufriere Hills volcano, Montserrat (Watts et al., 2002) which is consistent with the interpretation of low-frequency earthquakes beneath the same dome (Neuberg et al., 2006). The generally brittle nature of the dome and spine emplacement during the 2004–2008 eruption of Mt. St Helens (U.S.A.) has been compared with an apparently more viscous emplacement during the dome-forming 1980–1986 eruption (Sherrod et al., 2008). Mixed viscous-brittle emplacement has been explicitly inferred and modelled at the Santiaguito domes (Guatemala), with an emphasis on the Caliénte dome (Holland et al., 2011). And Mt. Unzen's (Japan) dome emplacements host fracture systems and were associated with seismicity, both indicative of fracturing during otherwise viscous emplacement (Lamb et al., 2015; Lavallée et al., 2022), consistent with dome emplacement scaling (Goto, 1999; Goto et al., 2020).

Clearly there is ample evidence for viscoelastic and mixed-mode viscous-brittle emplacement of dome lavas. However, leading theoretically-grounded rheological models for crystal-bearing magmas do not make predictions about bulk brittleness (Mueller et al., 2011; Mader et al., 2013; Truby et al., 2015). Instead, empirical fits to experimental data for deformation of real lavas at conditions of real dome emplacement have been forwarded (Lavallée et al., 2007; Avard and Whittington, 2012; Pistone et al., 2012). What is missing is a deep understanding of – and quantitative scaling for – the conditions under which mixed-mode viscous-brittle flow dominates, and therefore where laws such as that presented by e.g. Lavallée et al. (2007) are appropriate, versus the conditions under which purely viscous flow laws (Mueller et al., 2011; Mader et al., 2013) might be more appropriate descriptions.

To untangle the deformation regimes – purely viscous, mixed viscous-brittle, and purely brittle – requires a scaling for the conditions of shear stress, strain rate, and temperature under which a given lava will transition from one behaviour to another. Attempts have been made to do just this (Cordonnier et al., 2012a; Pistone et al., 2015; Wadsworth et al., 2018). However, those attempts are either confined to single or two-phase lava materials of melt or crystals-and-melt (Cordonnier et al., 2012a; Wadsworth et al., 2018; Vasseur et al., 2023) or they involve empirical steps and parameters that are 'tuned' to a given experimental dataset, such that it is not theoretical and therefore not easy to extrapolate to dome emplacement conditions with any confidence (Pistone et al., 2015; Coats et al., 2018). Despite formal avenues by which magma rheology can be rendered multiphase (Truby et al., 2015; Birnbaum et al., 2021), these approaches do not incorporate viscoelasticity and brittle onsets, and therefore the outstanding opportunity is to test these approaches against viscous-and-brittle data for which the transition is measured. Without such tests of theoretical models, we only have access to empirical multiparameter fits (Costa et al., 2009; Pistone et al., 2015) that are not useable in all conditions by geophysicists or those monitoring lava dome emplacement.

3. Materials and methods

For our experiments, we use a natural andesite from Volcán de Colima, an active stratovolcano in the Trans-Mexican Volcanic Belt in Mexico (Varley et al., 2019). From a single large ~ 0.8 m^3 pristine block, we produced cylindrical cores. This block is texturally similar to blocks
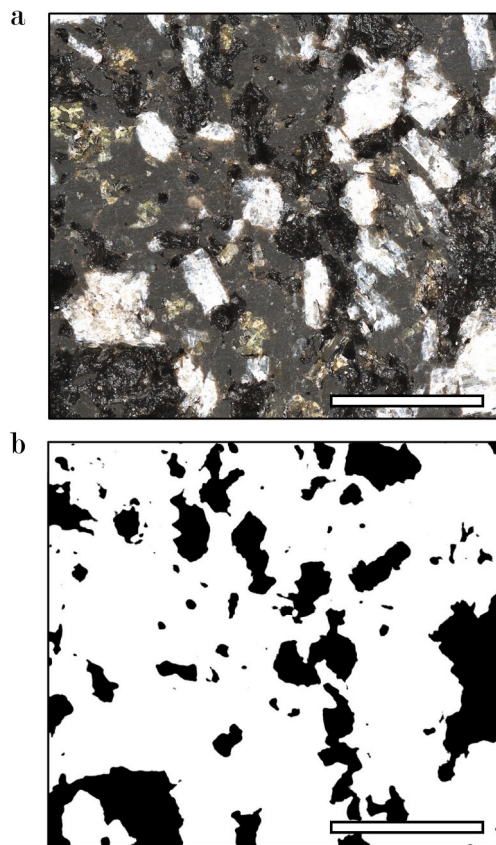
Fig. 3. Colima lava pre-experimental microtexture in (a) plane light (captured using a Keyence VK-X 1000 scanning microscope) and (b) processed so that the pores are isolated in black and the groundmass and phenocrysts in white. The scale bar in (a) is 500 μm long and (b) is at the same scale.

that have been used previously for experiments and was selected for its low fraction of microfractures (Lavallée et al., 2007). In Fig. 3 we show the microtexture of these samples using a Keyence VK-X 1000 scanning microscope at default settings in order to collect microtextural images of the pre-experimental samples, used to approximate the crystallinity and to detect fractures.

First, we cored six cylinders with a 20 mm diameter and 40 mm length in three orthogonal directions, to assess the initial permeability anisotropy of the block. Second, we cored six cylinders with 30 mm diameter and 60 mm length in three mutually perpendicular directions (2 cylinders per direction). Third, we cored three very large cylinders with 60 mm diameter and 120 mm length, in a single direction. And finally, we cored 24 small cylinders with 8 mm diameter and 5 mm length for low-stress rheology analysis as a control measure to test the purely viscous field of the rheology of this material. By using samples of different sizes, we can achieve these goals:

(1) Particularly small samples (8 mm diameter) for 'low-stress rheology' tests (see the description of the thermomechanical analyser below) are more likely to be in the purely viscous regime and allow us to examine deformation without brittle behaviour.
(2) Very large samples (60 mm diameter) for 'high-stress rheology' tests (see the description of the large hydraulic press below) allow us to check for permeability anisotropy development by sub-sampling the post-experimental samples.
(3) Moderately sized samples (20–30 mm diameter) for the same 'high-stress rheology' tests as in (2) can be used to map out the transition from purely viscous rheology at low stress to visco-elastic rheology at high stress.

3.1. Performing deformation experiments

We deformed three of the six 30 mm-diameter cylinders and all three of the 60 mm-diameter cylinders using a large, high-load uniaxial hydraulic press (manufactured by Voggenreiter GmbH and subsequently retrofitted by Instron™), which holds samples in the isothermal central portion of a 3-zone Gero™ furnace (for a full instrument description, see Hess et al., 2007). The strain data presented here are all corrected for system compliance by applying the same forces to the pistons without a sample; the system strain is subtracted from the measured strains. Heating at 0.5 K.s^{-1} we set the control temperature of the furnace at 1000°C, which resulted in a sample temperature of 950–960 °C as measured by thermocouples. This temperature range matches well the estimated eruption temperature for Volcán de Colima (Luhr, 2002). We used three thermocouples embedded in the sample itself at different positions to check for temperature homogeneity. After >5 hours equilibration time, the sample temperature was stable and spatially homogeneous to within ±3°C.

Previous work has shown that at low strain rates or low stresses, dome lavas flow viscously, while at high applied strain rates or stresses, dome lavas fail macroscopically (Lavallée et al., 2013; Kendrick et al., 2013; Coats et al., 2018). Therefore, we designed 'slow' and 'fast' experiments to explore both regimes. We applied a constant force on the sample, controlled by the upper piston and feedback with the load cell. Under constant force, the strain rate equilibrated to an approximately constant axial strain rate. The steady axial strain rate $\dot{\varepsilon}$ for the large samples (60 mm diameter), was stable at $\dot{\varepsilon} = 4.80 \times 10^{-3}$ s^{-1} at a force of 20 kN and an associated axial stress of 7 MPa – termed the 'fast' experiment – and stable at $\dot{\varepsilon} = 1.05 \times 10^{-3}$ s^{-1} at a force of 5 kN and associated stress of 1.7 MPa – termed the 'slow' experiment. For the 30 mm and 8 mm samples, these 'fast' and 'slow' values of $\dot{\varepsilon}$ are different and scale with the sample cross-sectional area (we applied the same driving axial stresses). In Fig. 4, we demonstrate that the axial strain rate is constant to within a tolerance of 3 % of the strain rate and this tolerance is propagated into uncertainties on parameters that rely on $\dot{\varepsilon}$ used later. We continuously recorded the position of the upper piston and the load. The experiments were halted once the axial strain of the sample cylinder reached 0.2. While this strain was nominally slightly larger than the computed 0.2 after the samples had cooled, it was consistent from test-to-test, which was the aim here. Once the experiment was complete, the piston was retracted from the sample, and a slow cooling ramp was initiated at 0.05 K.s^{-1} to minimize microcracking by thermal stresses, which can occur during the cooling of volcanic rocks (Griffiths et al., 2024).

We monitored the acoustic emission signals emitted during the experiments using two broadband transducers (of 125 kHz central frequency) attached to the cooler ends of the pistons (cf Vasseur et al., 2018). The signals were transferred using buffered 40 dB preamplifiers to a data acquisition system (Richter system, from Applied Seismology Consulting), which recorded acoustic emission voltage data continuously at a sampling rate of 10 MHz, synchronized with the mechanical data acquisition.

The additional 24 experiments using small 8 mm diameter cylinders were performed in a Netzsch Pegasus 404c thermomechanical analyser (TMA). The temperature of these experiments was varied in the range 875–1050 °C, encompassing the predicted eruption temperature range, and a hold time of 20 min was allowed for thermal equilibrium before deformation was applied. These experiments were set up differently from the high-load press tests described above, such that the force of the piston assembly on the sample cylinders was held constant at very low loads of either 0.1, 1.3, 2.5, 2.7, or 3.0 N depending on the experiment. The force was held at one of these values until a strain of 0.2, which in all cases was sufficient to allow the rate of deformation to stabilize to a steady rate of strain, $\dot{\varepsilon}$. The stabilized axial rates were in the range $2.44 \times 10^{-6} < \dot{\varepsilon} < 7.3 \times 10^{-4}$ s^{-1}, substantially lower than in the tests on the
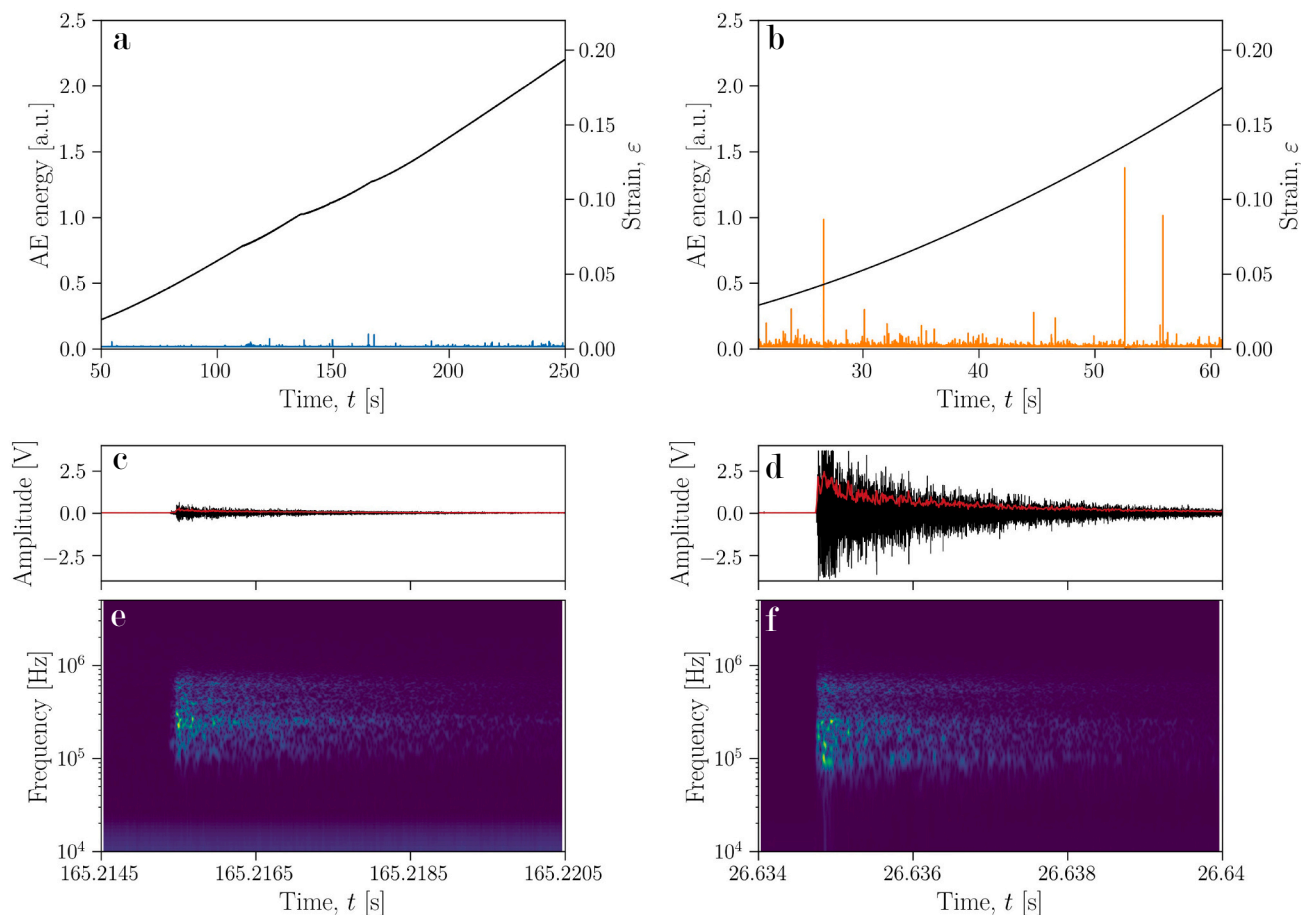
Fig. 4. Colima lava physical and rheological results. (a-b) The mechanical and acoustic dataset presented here collected during high-temperature deformation tests (60 mm diameter samples). Panels (a) and (b) show the axial strain ε (black curve) and the continuous root-mean-square of the acoustic emission signal (in blue and orange, respectively) using a sliding and an averaging window of 10 s and 1 ms, respectively, with time t for (a) the 'slow experiment' and (b) the 'fast experiment'. Panels (c) and (d) show a representative example waveform of a single acoustic event from each experiment for which the black curve shows the amplified voltage amplitude recorded at the sensor, and the red curve represents its root-mean-square using an averaging window of 10 μs. Panels (e) and (f) show the spectrogram for the events shown in (c) and (d). (For interpretation of the references to colour in this figure legend, the reader is referred to the web version of this article.)

larger samples described above. These samples were then cooled slowly under no load for post-experimental analysis. The monitoring of acoustic emissions was not possible in this experimental setup.

In both experiment types (those using the high-load press and those using the TMA at low-load), we use a < 10 μm grain size alumina ceramic powder on the sample top and sample bottom. This powder ensures perfect slip conditions between the pistons and the samples, which allows us to avoid complex corrections for inhomogeneous sample deformation (e.g. Gent, 1960).

3.2. Measuring porosity and permeability

We measured the sample geometrical volume of the 30 mm-diameter cylinders which, with the sample mass, was used to compute the bulk density. We also measured the inaccessible volume of the samples by helium pycnometry using an Ultrapyc 3000 from Anton Paar™. Finally, we measured the density of an aliquot of powdered material from the same sample block, which in turn allowed us to compute the isolated, total, and connected porosity (calculation methods given in previous work; Heap et al., 2017). The dominant uncertainty on these determinations arises from the sample volume and mass, which results in a relative approximate error of < 1% for porosity; measurement uncertainty calculations are presented elsewhere (Vairé et al., 2024). We then used a nitrogen gas desktop permeameter from Vinci Technologies™ to measure the permeability using a suite of individual flow-through

experiments. We measured the permeability of the intact 20 mm-diameter samples, and the permeability of the 8, 30, and 60 mm-diameter samples following high-temperature deformation. Prior to measurements of permeability, the deformed samples that were initially 8 mm in diameter were re-cored to 7 mm diameter, removing the slight surface irregularities induced by the deformation, and similarly the initially 30 mm diameter cores were re-cored to a diameter of 20 mm. For these sample suites, permeability was measured along their axis (i.e. in the direction they were deformed). For the deformed samples that were initially 60 mm in diameter, we cored 20 mm-diameter sub-samples in the three orthogonal directions. For each flow-through experiment in the permeameter, we set an upstream gas pressure P_1 and the downstream gas pressure P_2 was the atmospheric pressure in the laboratory. A confining pressure P_c of 1 MPa (nitrogen gas) was first applied to a jacketed (silicone rubber) sample. The sample was then left at 1 MPa confinement for 1 h to ensure microstructural equilibrium. The measured variable was the average steady-state fluid velocity q calculated from a steady-state volumetric flow rate Q and the cross-sectional area of the sample A via $q = Q/A$. The permeability k was determined using $k = 2q\mu_f L P_2 / (P_2^2 - P_1^2)$ for compressible gas flow, where μ_f is the viscosity of the pore fluid (nitrogen gas; $\mu_f \approx 1.8 \times 10^{-5}$ Pa.s), and L is the sample length (Kushnir et al., 2017b). We constrain k for a wide range of ΔP to confirm that k is in the Darcian regime at low Reynolds number. Low Reynolds number flow was ensured by checking for the necessity of a Forchheimer correction to the

Table 1
Chemical composition of groundmass glass.

	5 μm defocussed beam	Standard deviation	10 μm defocussed beam	Standard deviation
	$n = 14$		$n = 5$	
SiO_2	72.64	0.50	72.28	0.88
TiO_2	0.91	0.05	0.86	0.05
Al_2O_3	12.86	0.12	12.94	0.17
FeO*	3.31	0.14	3.31	0.08
MnO	0.06	0.04	0.05	0.05
MgO	0.33	0.05	0.33	0.04
CaO	0.95	0.09	1.09	0.15
Na_2O	3.74	0.23	3.96	0.11
K_2O	3.63	0.10	3.44	0.21
P_2O_5	0.14	0.02	0.16	0.05
Total**	98.56	0.44	98.42	0.97

* All Fe assumed to be FeO for the purposes of calculation. Fe speciation is not constrained.

** Totals that are 95 % or less are removed.

permeability; this procedure is documented in detail in Heap et al. (2017). We take the arithmetic mean of the repeat determinations of k and compute the standard error on those averages, which is larger than the uncertainty on any of the input parameters for k determination (Heap et al., 2017; Vairé et al., 2024).

3.3. Measuring groundmass glass geochemistry

We measured the composition of the groundmass glass in a polished section of the starting material using a Cameca SX100 electron probe microanalyser (Table 1). We did this using two different sets of operating conditions: (1) 15 kV accelerating voltage, 5 nA current, and a 5 μm defocused beam, and (2) 15 kV accelerating voltage, 2 nA, and a 10 μm defocused beam. These two settings were used to check for loss of light elements such as sodium at the higher current and smaller beam. In Table 1 we report a summary of the glass composition of our samples.

4. Laboratory results

The selected andesitic dome rock, has approximately 0.55 ± 0.02 area fraction crystals (dense rock equivalent; Fig. 3a) and 0.17 ± 0.02 total porosity (measured by pycnometry, consistent with 0.18 ± 0.03 from 2D image analysis; Fig. 3b).

The sample material was used in high-temperature high-load uniaxial deformation tests at $940 \pm 4^\circ C$ (Hess et al., 2007) at two stresses (as noted above): (1) a 'fast experiment' (higher load) and (2) a 'slow experiment' (lower load). The bulk response of the samples to a high stress σ is to undergo inelastic permanent axial strain ε. This strain is accumulated at approximately a constant rate over the strain interval investigated here (Fig. 4a and b). We therefore attribute a single strain

rate $\dot{\varepsilon}$ to each experiment; for the large samples (60 mm diameter), $\dot{\varepsilon} = 4.80 \times 10^{-3}$ s^{-1} for the fast experiment, and $\dot{\varepsilon} = 1.05 \times 10^{-3}$ s^{-1} for the slow experiment (this is different, but known, for the smaller samples). Here, we show the examples for the large 60 mm samples (Fig. 4a & b). For the 30 mm samples, we tested the same range of axial stresses by reducing the applied forces proportional to the sample cylinder circular cross-sectional area, so that we achieved similar deformation curves as shown in Fig. 4a & b, and therefore so that the axial strain rates covered the same range. Importantly, we note that macroscopic (sample-scale) failure did not occur during any experiment. Using the observed strain data, there is no indication (e.g., stress drops) that the sample deformation included anything but viscous flow mechanisms at the local micro-mechanical scales.

While the mechanical data from the experiments may suggest viscous flow, it is important to identify the micromechanical textural changes in the samples that can be used to infer the mechanism by which the samples accommodate strain during apparent flow. After the fast experiment at the higher applied stress, we find that the groundmass between the phenocrysts hosts noticeably far more micro-fractures than were present prior to the experiments (Fig. 5). Such fractures are not present in the post-experimental samples for the slow experiments (Fig. 5). For both the fast and slow experiments, we find that acoustic emission activity, a proxy for microcrack formation and growth (Lockner, 1993), occurs in bursts throughout the experiment at high temperatures (Fig. 4a and b). Each burst represents a waveform with a discrete sharp onset and decay (Fig. 4c and d) and a dominant frequency content between 10^5 and 10^6 Hz (Fig. 4e and f). The bursts in acoustic emission energy and the amplitude of each event are higher magnitude for the fast experiment compared with the slow experiment (Fig. 4). We note that the amplitude of the events is only used for event-to-event and experiment-to-experiment relative comparisons. This suggests that the fast experiments show more micro-cracking events than the slow experiments and that those micro-cracking events are larger in amplitude. This appears consistent with the obvious textural evidence for microfractures in the post-experimental samples from the fast experiments. Similar post-experimental observations have been made on experimentally deformed dome lavas (Lavallée et al., 2007, 2013; Kendrick et al., 2013, 2017; Coats et al., 2018).

Our 24 very low-stress (at 0.1–3 N load and 2–60 kPa axial stress) tests performed on the small 8 mm samples act as a control dataset. The measured strain rates are substantially lower when compared with the tests on the larger samples, and are far lower than most conventional rheology experiments on similar dome samples from Volcán de Colima (Lavallée et al., 2007; Kendrick et al., 2013), and as such a purely viscous response can be expected. In all cases, the samples reached a steady state strain rate for the applied stress, and we observed no evidence for anything but purely viscous flow during these control tests, even when examining the groundmass textures after the experiments.

The permeability of the samples was initially near isotropic (i.e.,
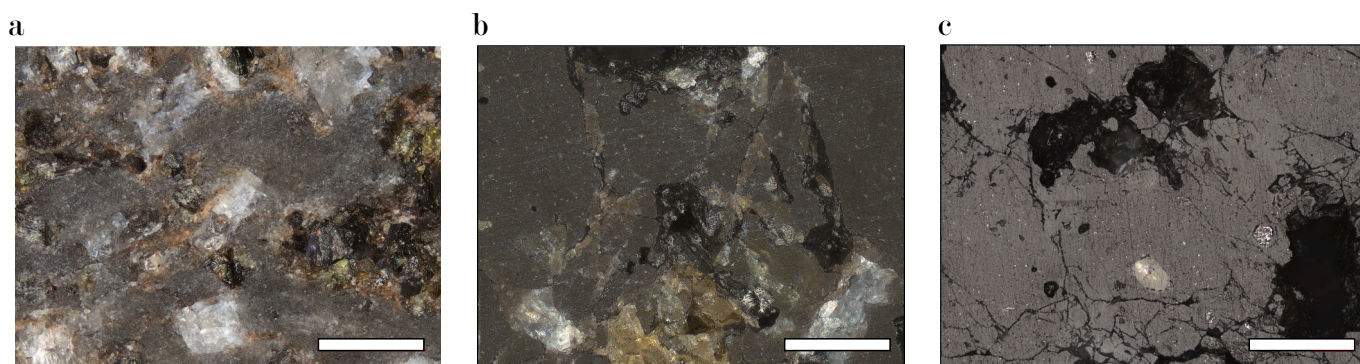

Fig. 5. Post-experimental sample textures in (a-b) plane light and (c) reflected light (captured using a Keyence VK-X 1000 scanning microscope). (a) A sample that was deformed during 'slow' deformation (see text). (b) and (c) samples deformed during 'fast deformation' (see text). All scale bars are 500 μm.
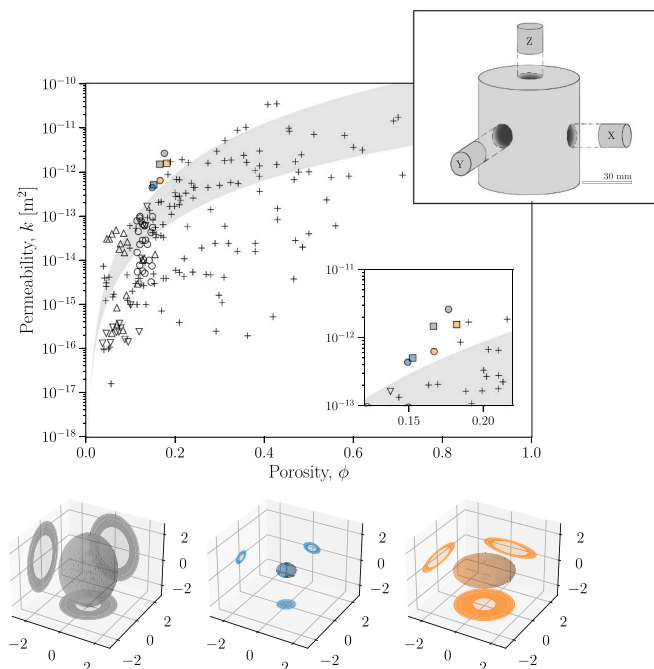
Fig. 6. The permeability of our samples before and after high-temperature deformation to low ($\varepsilon = 0.2$) axial strain. Here we show the pre-experimental sample in grey, the post experimental sample for the 'slow experiment' in blue, and the post experimental sample for the 'fast experiment' in orange (as in Fig. 2). The circles represent the permeability in the axial direction (z), and the squares represent the mean of the permeability in the two radial directions (y and x; the range between the two values is smaller than the point). We also show the results of the 24 smaller samples where the post-experiment permeabilities could only be measured in the axial direction (unfilled circles). Uncertainties on the permeability and porosity determinations are smaller than the data points shown. We also show the compiled suite of volcanic rock permeabilities for the products of effusive eruptions (crosses; Colombier et al., 2017) and the proposed $k(\phi)$ empirical laws (Mueller et al., 2005) of the form $k = k_0\phi^n$ with $k_0 = 1 \times 10^{-17}$ m^2 bounded by $n = 3$ and $n = 3.8$ (these two empirical laws are given by the upper and lower bounds on the grey area). For instructive comparison, we also give data for banded Colima dome rocks that show significant anisotropy between the band-parallel direction (upward triangles) and band-perpendicular direction (downward triangles; Farquharson et al., 2016). *Inset*: a zoom-in on the data in the main plot. Below we show anisotropy ellipsoids where the axes values are given in darcy, rather than m^2, simply for clarity (1 darcy is approximately 1×10^{-12} m^2). These ellipsoids are designed to be illustrative of the degree of anisotropy, such that the relative shape change is of particular interest. (For interpretation of the references to colour in this figure legend, the reader is referred to the web version of this article.)

equal in the three orthogonal directions of measurement) and consistent with values defining the high end of the range of natural dome lavas previously measured (Mueller et al., 2005; Farquharson et al., 2016; Colombier et al., 2017). Initially, the permeability in three orthogonal directions was 2.62×10^{-12} m^2 in the axial direction (directions quoted with respect to the high-temperature deformation experiments), and 1.45×10^{-12} m^2 and 1.07×10^{-12} m^2 in the two perpendicular radial directions, respectively. The average initial permeability was therefore 1.71×10^{-12} m^2 (see Fig. 6 *inset*). For the 60 mm samples deformed at 1.7 MPa stress (slow experiments), the porosity and permeability in all three orthogonal directions decreased isotropically and steeply, tracing out a general trend broadly similar to the empirical power-law trend proposed for effusive eruptive products including dome lavas (Mueller et al., 2005). The deformation at this low stress appears to reduce the small initial permeability anisotropy, resulting in isotropic densification and an isotropic end-state of lowered permeability, as also observed in samples of deformed porous rhyolite. By contrast, the experiments

performed at the higher 7 MPa stress result in samples for which the vertical component of the permeability (parallel to the deformation axis; z-direction) decreased by the same amount as in the slow experiments, whereas the permeability in the two orthogonal directions perpendicular to the deformation axis (radial-direction) did not change substantially (Fig. 6). This results in anisotropic permeability for the samples deformed at higher stress (consistent with the conceptual framework presented by Lavallée et al. (2013) and by Kendrick et al. (2013)). Finally, the small-sample low-load 'purely viscous' tests resulted in low permeabilities that straddle much of the range expected for Volcán de Colima dome rocks at these porosities (Farquharson et al., 2015). All processed experimental data are in Table 2.

5. Interpretation and scaling

The laboratory results show that, at moderate strain rates, dome lavas can exhibit evidence for macroscopic viscous flow (Fig. 4a and b), yet simultaneously generate acoustic emissions indicative of micro-cracking (Fig. 4c and d). The slow (lower stress) experiments showed substantially fewer acoustic emission events, with typically lower amplitudes, compared with the fast (higher stress) experiments (Fig. 4), suggesting that there is a strain-rate dependence of the fracturing process. This is consistent with the observation that slow deformation results in an isotropically reduced permeability, indicating a viscous compaction process, whereas the fast experiments result in the development of permeability anisotropy, consistent with fracturing in the anisotropic stress field of our experiments. At low strain rates, dome lavas flow viscously, while at high strain rates dome lavas fail macroscopically and this strain rate dependence influences the number and energy of acoustic events released (Lavallée et al., 2008, 2013; Wadsworth et al., 2018). Therefore, we propose that our 'fast' and 'slow' results sit at a transition between a predominantly viscous response in which no acoustic emissions would be expected, and a macroscopically brittle response in which the sample would fail.

5.1. A two-phase crystal-bearing scaling for brittleness

In order to scale for the conditions that relate to viscous, mixed viscous-brittle, and brittle responses to applied stresses or strain rates, we apply and extend a viscoelastic framework (Cordonnier et al., 2012b; Wadsworth et al., 2018). We define two timescales: (1) a timescale over which the melt phase can relax shear stresses $\lambda_r = \mu/G$, where μ is the melt viscosity and G is the shear modulus in the elastic regime (i.e. typically measured at very high oscillation frequency); (2) a timescale characteristic of the deformation $\lambda = 1/\dot{\gamma}$, where $\dot{\gamma}$ is the shear strain rate. For any cylindrical sample deformed axially, we use the Trouton rule: $3\dot{\varepsilon} = \dot{\gamma}$ implying perfect slip with the pistons (see Methods). The difference between this and a no-slip assumption is minor (Wadsworth et al., 2018). The ratio between these two timescales is a Weissenberg number $\mathrm{Wi} = \lambda_r/\lambda = \mu\dot{\gamma}/G$, such that $\mathrm{Wi} \ll 1$ is the viscous field in which shear stresses can be relaxed on the timescale of deformation, and $\mathrm{Wi} \gg 1$ is the brittle field in which shear stresses cannot be relaxed. Note that the Deborah number is the oscillatory counterpart to the Weissenberg number and is sometimes used in the volcanological literature interchangeably with the Weissenberg number (which pre-supposes that the Cox-Merz rule holds; see Section 5.2 of Mader et al. (2013) for a discussion). The specific transition between the two fields – brittle and viscous – is Wi_c and has been experimentally determined to differ from unity and takes a value $0.01 \leq \mathrm{Wi}_c \leq 0.04$ for single-phase silicate melts (Webb and Dingwell, 1990; Cordonnier et al., 2012b; Wadsworth et al., 2018).

For silicate melts that suspend crystal phases, the effective strain rate in the melt $\dot{\gamma}'$ is higher than the bulk strain rate simply because the crystals are rigid and not accommodating large proportions of the strain (Vasseur et al., 2023). Using data from Cordonnier et al. (2012a),

Table 2
Experimental conditions and results.

Initial porosity	Initial permeability (x-direction)	Initial permeability (y-direction)	Initial permeability (z-direction)	Crystallinity
-	m^2	m^2	m^2	-
0.16; 0.17; 0.17	1.45×10^{-12}	1.52×10^{-12}	2.62×10^{-12}	~ 0.55

Instrument	Sample radius	Sample length	Temperature	Load	Axial strain rate	Wi (melt only)	Wi (crystal-bearing)*	Brittle?**	Final porosity***	Final permeability (x-direction)	Final permeability (y-direction)	Final permeability (z-direction)$
	mm	mm	K	N	s^{-1}	-	-	-	-	m^2	m^2	m^2
Uniaxial press	29.94	105.26	1233		1.05×10^{-3}	1.20×10^{-4}	4.29×10^{-4}	No	0.155; 0.15; 0.149	4.22×10^{-13}	5.95×10^{-13}	4.41×10^{-13}
Uniaxial press	29.98	103.80	1224		4.79×10^{-3}	1.97×10^{-5}	2.61×10^{-3}	Yes	0.182; 0.155; 0.167	1.57×10^{-12}	1.51×10^{-12}	6.33×10^{-13}
Uniaxial press	14.02	59.19	1231		2.23×10^{-3}	4.89×10^{-6}	6.88×10^{-4}	No				
Uniaxial press	14.11	57.95	1228		1.10×10^{-2}	2.20×10^{-4}	3.09×10^{-3}	Yes				
Uniaxial press	14.01	59.26	1228		7.71×10^{-3}	1.69×10^{-4}	2.83×10^{-3}	Yes				
TMA#	4.00	5.00	1148	3	3.11×10^{-6}	1.17×10^{-6}	1.65×10^{-5}	No	0.17			5.98×10^{-14}
TMA	4.00	5.00	1173	3	5.22×10^{-6}	7.62×10^{-7}	1.07×10^{-5}	No	0.17			7.82×10^{-14}
TMA	4.00	5.00	1198	3	1.19×10^{-5}	7.13×10^{-7}	1.00×10^{-5}	No	0.17			6.35×10^{-14}
TMA	4.00	5.00	1198	3	9.80×10^{-6}	5.87×10^{-7}	8.25×10^{-6}	No	0.17			9.02×10^{-14}
TMA	4.00	5.00	1198	3	2.24×10^{-5}	1.34×10^{-6}	1.89×10^{-5}	No	0.17			4.49×10^{-14}
TMA	4.00	5.00	1198	3	3.10×10^{-5}	1.86×10^{-6}	2.61×10^{-5}	No	0.17			2.28×10^{-14}
TMA	4.00	5.00	1198	3	1.35×10^{-5}	8.08×10^{-7}	1.14×10^{-5}	No	0.17			5.70×10^{-15}
TMA	4.00	5.00	1223	3	3.91×10^{-5}	1.01×10^{-6}	1.42×10^{-5}	No	0.17			2.86×10^{-14}
TMA	4.00	5.00	1223	2	1.11×10^{-5}	2.87×10^{-7}	4.03×10^{-6}	No	0.17			7.45×10^{-15}
TMA	4.00	5.00	1223	2.5	1.79×10^{-5}	4.62×10^{-7}	6.50×10^{-6}	No	0.17			5.52×10^{-15}
TMA	4.00	5.00	1223	1.3	1.62×10^{-5}	4.18×10^{-7}	5.88×10^{-6}	No	0.17			9.82×10^{-14}
TMA	4.00	5.00	1223	3	3.99×10^{-5}	1.03×10^{-6}	1.45×10^{-5}	No	0.17			5.08×10^{-15}
TMA	4.00	5.00	1223	2.7	3.42×10^{-5}	8.83×10^{-7}	1.24×10^{-5}	No	0.17			2.83×10^{-14}
TMA	4.00	5.00	1223	3	3.60×10^{-5}	9.03×10^{-7}	1.31×10^{-5}	No	0.17			1.03×10^{-14}
TMA	4.00	5.00	1243	3	7.00×10^{-5}	9.54×10^{-7}	1.34×10^{-5}	No	0.17			7.69×10^{-14}
TMA	4.00	5.00	1248	3	7.82×10^{-5}	9.13×10^{-7}	1.28×10^{-5}	No	0.17			9.71×10^{-14}
TMA	4.00	5.00	1248	3	7.76×10^{-5}	8.94×10^{-7}	1.26×10^{-5}	No	0.17			2.30×10^{-14}
TMA	4.00	5.00	1248	2	4.79×10^{-5}	5.59×10^{-7}	7.68×10^{-6}	No	0.17			9.95×10^{-15}
TMA	4.00	5.00	1248	0.1	2.44×10^{-6}	2.85×10^{-8}	4.01×10^{-7}	No	0.17			4.31×10^{-14}
TMA	4.00	5.00	1273	3	1.52×10^{-4}	8.37×10^{-7}	1.18×10^{-5}	No	0.17			6.61×10^{-14}
TMA	4.00	5.00	1273	3	1.01×10^{-4}	5.56×10^{-7}	7.82×10^{-6}	No	0.17			5.51×10^{-14}
TMA	4.00	5.00	1323	3	7.00×10^{-4}	9.61×10^{-7}	1.35×10^{-5}	No	0.17			1.51×10^{-14}
TMA	4.00	5.00	1323	3	7.21×10^{-4}	9.90×10^{-7}	1.39×10^{-5}	No	0.17			3.23×10^{-15}
TMA	4.00	5.00	1323	3	6.54×10^{-4}	8.98×10^{-7}	1.26×10^{-5}	No	0.17			7.76×10^{-15}

* Computed assuming $\phi_x = 0.55$ and $\phi_m = 0.7$.

** Based on either post-experimental textural evidence or in-situ acoustic signals.

*** Where this is a large sample (30 mm radius) three values are given denoting the porosity for the sub-samples in the x, y, and z directions; note that these are simply the scalar porosity values that relate to the 3 permeability values also given in this table.

$ For most samples, the permeability in the z direction is the only value measured.

TMA is 'thermomechanical analysis'.

Wadsworth et al. (2018) proposed a scaling relationship between the applied $\dot{\gamma}$ and an expected $\dot{\gamma}'$ in the melt between crystals as

$$\dot{\gamma}' = \frac{1}{\lambda'} = \dot{\gamma}\left(1 - \frac{\phi_x}{\phi_m}\right)^{-1} \qquad (1)$$

where ϕ_x is the suspended crystal volume fraction, and ϕ_m is a maximum packing of crystals in the melt. In Fig. 7a and b we illustrate the principle represented by Eq. (1). For crystal-bearing magma, $\dot{\gamma}'$ should replace $\dot{\gamma}$ in the definition of Wi, with the anticipated result that when $\phi_x = 0$, $\dot{\gamma}' = \dot{\gamma}$.

Cordonnier et al. (2012a) suggested that the melt viscosity in Wi should be replaced with the bulk apparent viscosity of the suspension η (consistent with discussion of the so-called 'lever function' by Vasseur et al., 2023). This results in a different definition of the Weissenberg number which is $Wi = \eta\dot{\gamma}/G$. When Eq. (1) is also used then we can exchange $\dot{\gamma}$ for $\dot{\gamma}'$; taken together, this results in a scaled Weissenberg number $Wi' = \eta\dot{\gamma}'/G$ with the critical value at $Wi'_c = 0.01$, which accounts for the effect of crystals on the critical brittleness threshold.

Using our new experimental data, in Fig. 8 we show that the scaling proposed above accurately demarcates brittle from viscous results. To show that this scaling works more generally across different systems, we compile existing experimental results in which crystal-bearing lavas of known starting phase proportions were heated and deformed uniaxially (Lavallée et al., 2007, 2013; Kendrick et al., 2013; Coats et al., 2018; Wadsworth et al., 2018), triaxially (Tuffen et al., 2008), or under torsion (Pistone et al., 2012; Cordonnier et al., 2012a). In Fig. 8, we show this new compilation of existing deformation results for crystal-bearing silicate melts are also well demarcated by the scaling proposed here. The scaling given above does not account for the effect of porosity, and so, given that some of the compiled data are for porous materials, a natural extension to this approach would be to include that effect.

5.2. An extension to the three-phase brittle threshold

The premise of Eq. (1) is that all of the strain in the melt is taken up in the space that is not occupied by either the crystals, or the melt that would exist between maximally packed crystals of the same type. We can use this same logic to propose a simple method to account for small amounts of gas (in pores and bubbles) in the magma. In a crystal-free melt, a simple approach is to assume that this would lead to a scaling for the strain rate as $\dot{\gamma}' = \dot{\gamma}(1 - \phi)^{-1}$, where ϕ is the gas volume fraction (Fig. 7c). In order to combine this gas volume scaling with Eq. (1), we need to take an effective medium approach such that we apply Eq. (1) only to the gas-free (solid) portion of the system. To do this, we define a crystallinity on a pore free basis (i.e. 'dense rock equivalent' or DRE), termed ϕ'_x and given by

$$\phi'_x = \frac{\phi_x}{1 - \phi}; \quad \phi_x = \phi'_x(1 - \phi). \qquad (2)$$

Then, we take two steps: first we inject Eq. (2) into Eq. (1), and second, we additionally multiply by the scaling for the strain rate amplification due to the gas phase, which we propose is proportional to $(1 - \phi)^{-1}$ (Fig. 7c). These two steps lead to a multiphase scaling for the scaled strain rate as

$$\dot{\gamma}' = \frac{1}{\lambda'} = \dot{\gamma}\left(1 - \frac{\phi'_x}{\phi_m}\right)^{-1}(1 - \phi)^{-1}. \qquad (3)$$

If crystallinity is reported on a pore-free basis (i.e. dense rock equivalent; DRE), then Eq. (3) holds. Via Eq. (2), Eq. (3) is identical to

$$\dot{\gamma}' = \frac{1}{\lambda'} = \dot{\gamma}\left[1 - \frac{\phi_x}{\phi_m}(1 - \phi)^{-1}\right]^{-1}(1 - \phi)^{-1} \qquad (4)$$

valid for when crystallinity is reported on a bulk basis (i.e., crystal volume fraction relative to the total magma volume). In Eqs. (3) (crystallinity on a DRE basis) and 4 (crystallinity on a total volume basis), we
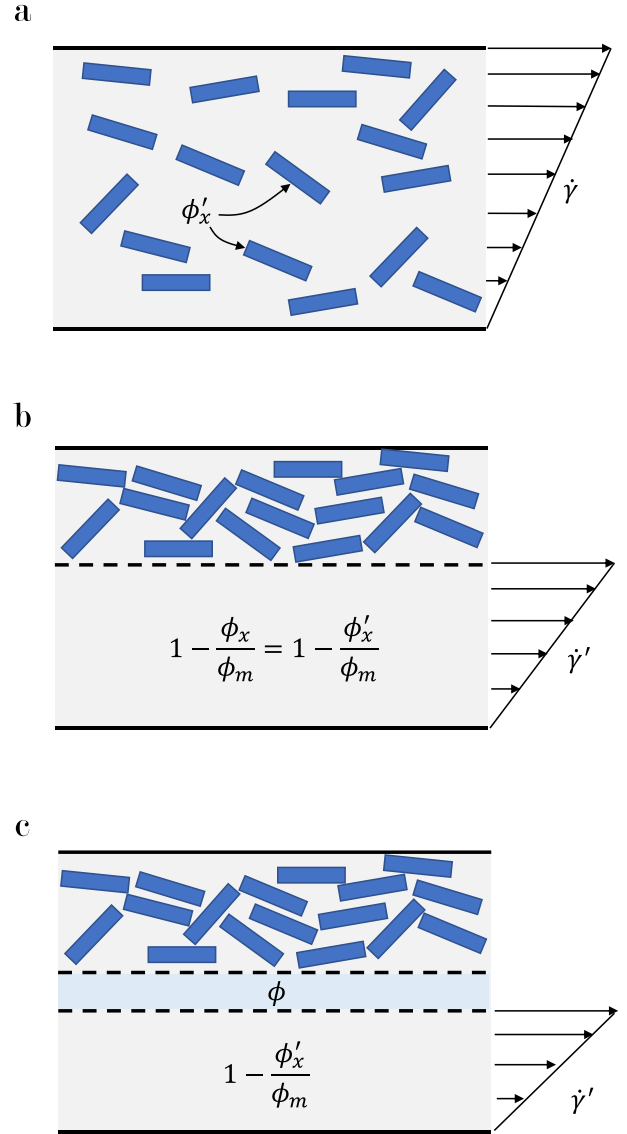

Fig. 7. An abstract visual depiction of the effect of the scaling approaches for the effective strain rate invoked here. (a) No scaling where the strain rate is bulk applied strain rate. (b) A two-phase scaling for the strain rate in the melt in a crystal-bearing magma where $\dot{\gamma}' \propto \phi_x/\phi_m$. (c) A simplistic approach to a multiphase scaling for the strain rate in the melt in a crystal- and bubble-bearing magma where $\dot{\gamma}'$ is additionally proportional to the porosity ϕ.

assume that the gas volume fraction would always be reported relative to the total magma volume (i.e., a porosity). Eqs. (3) and (4) represent a multiphase approach to how strain rate is partitioned between phases (pores and crystals) in a magma.

5.3. Testing the brittle threshold against datasets

The partitioning of strain rates between rigid (crystal) phases and deformable (gas) phases is poorly understood, and therefore Eqs. (1)–(4) are suggested scaling approaches built on a relatively simplistic approach. For this reason, they require testing against experimental data. Our experimental data new to this work involves analysis of one sample-type with one porosity (0.17), and so it is important that we additionally analyze existing data with a wider range of porosity.

First, Coats et al. (2018) report experiments in which cylindrical samples from Mt. Unzen were heated and deformed uniaxially using the same technique we employ in this study. These experiments cover the
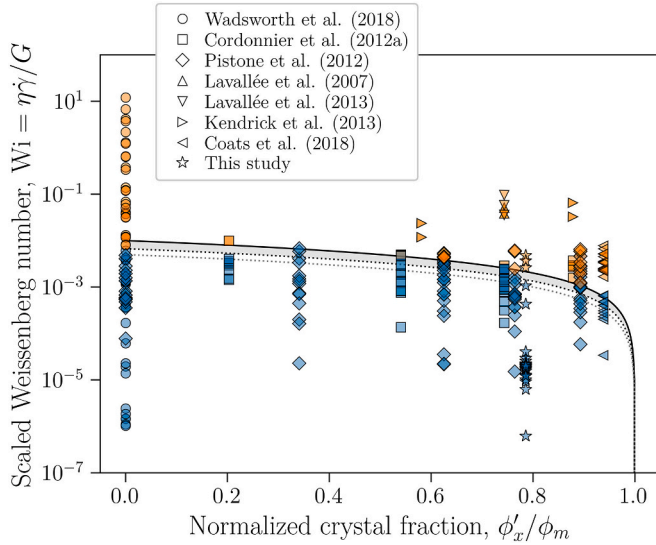
Fig. 8. Testing a multiphase viscous-to-brittle flow threshold via a compilation of existing experimental data. We show experimental data for the torsional deformation of synthetic melts containing crystals (Cordonnier et al., 2012a), and synthetic melts containing crystals and a gas phase (Pistone et al., 2012), and the uniaxial deformation of Volcán de Colima dome lavas (Lavallée et al., 2007, 2013; Kendrick et al., 2013), Mt. Unzen (Japan) dome lava samples (Coats et al., 2018) and obsidian (Wadsworth et al., 2018). For experimental data, we define $\mathrm{Wi} = \dot{\gamma}\eta/G$ after Cordonnier et al. (2012a) using the published values of $\eta = \sigma/\dot{\gamma}$ where σ is the deforming stress and $\dot{\gamma}$ is the resultant shear strain rate. We take $G = 10^{10}$ Pa in all cases. For this study and for Cordonnier et al. (2012a), and Pistone et al. (2012) $\phi_m = 0.74$, and for Coats et al. (2018) $\phi_m = 0.8$. The samples are identified as viscous (blue) or brittle (orange) based on either the reports of the original study or based on examination of the raw data (Materials and Methods). The black curve is the proposed viscous-to-brittle threshold $\mathrm{Wi_c} = 1 - \phi'_x/\phi_m$ (thereby taking the dense rock equivalent). The grey band is a lower bound given by Eq. (3) with $\phi = 0.33$ (black dotted line). The curve for $\phi = 0.5$ (grey dotted line) is also given, showing that the effect of these low porosities is negligible. (For interpretation of the references to colour in this figure legend, the reader is referred to the web version of this article.)

range $0 < \phi \leq 0.33$ and $0 < \phi_x \leq 0.5$ with those authors reporting a lower limit ϕ_m of 0.76 (Coats et al., 2018).

Second, Pistone et al. (2012) deformed a synthetic melt-supported suspension of crystals and gas bubbles, and present experimental results for the measured shear stress τ as a function of shear strain $\dot{\gamma}$ (e.g. their Fig. 3). Sawtooth-form results are interpreted as the result of fracture-and-healing cycles in the experiment. This was tested explicitly in a similar torsion device by Kushnir et al. (2017a) and found instead to possibly be the result of a repeated slip on the piston assembly. On that basis, our interpretation of their flow curves is micro-mechanically brittle if

(1) The flow curves exhibit a large non-recoverable stress drop during strain. We interpret this to represent an experiment that has experienced a micro-fracturing component to the deformation (e. g. experiment P1262 at $\dot{\gamma} = 2.1 \times 10^{-3}$ s^{-1});

(2) The flow curves exhibit small but continuous intermittent stress drops observed during strain (e.g. experiment P1268 at $\dot{\gamma} > 1.91 \times 10^{-3}$ s^{-1});

(3) The flow curves show strain hardening (e.g. experiment P1198 at $\dot{\gamma} = 1.04 \times 10^{-3}$ s^{-1}), which we interpret as representing a change in the microstructure not seen in non-fracturing magma-analogue rheology (Mueller et al., 2011).

Criterion (1) is consistent with the original interpretations of Pistone et al. (2012), criterion (2) is consistent with direct observations in

uniaxial compression (Coats et al., 2018; Wadsworth et al., 2018), and criterion (3) is consistent with an interpretation by Coats et al. (2018) that such hardening in natural samples may be associated with transitional mixed brittle-viscous flow. This reinterpretation exercise allows us to estimate λ'_r and λ' for a sub-set of the full dataset for which the flow curves $\tau(\gamma)$ are shown visually in Pistone et al. (2012). In summary, Pistone et al. (2012) cover the range $\phi \leq 0.12$ and $\phi_x \leq 0.65$. Pistone et al. (2015) give an estimated limit ϕ_m of 0.74. In Fig. 8 we show that, in all cases, these data show good agreement with the scaling for the transition from a viscous to a micro-fracturing regime proposed here.

Third, Lavallée et al. (2007), Lavallée et al. (2013), and Kendrick et al. (2013) all report data for the viscosity as a function of applied uniaxial stressing of samples from Volcán de Colima. Those authors all report some post-deformation sample images that show evidence for brittle deformation in response to stress. For example, Fig. 2 in Lavallée et al. (2007) shows that at ~ 30 MPa axial stress, their sample responded with brittle deformation under uniaxial conditions; therefore, for any experimental condition at this stress or greater, we categorize the samples within the brittle field. Similarly, figures DR3 and DR8 in Lavallée et al. (2013) demonstrate that their sample deformation at ~ 28 MPa, ~ 46 MPa, and ~ 76 MPa axial stress can all be attributed to the brittle field. Finally, Fig. 7 in Kendrick et al. (2013) shows that the sample LAH4 exhibited a brittle response when deformed at ≥ 12 MPa axial stress. The crystallinities and porosities for these samples are all quoted in the originating sources and we use $\phi_m = 0.75$ for these data, consistent with both Caricchi et al. (2007) and the data for our andesite from Volcán de Colima presented herein.

In all data analysed here, we take the measured viscosity reported in the study originating the data when defining λ_r or η in the variants of the Weissenberg number reported, meaning that we do not rely on a specific assumption of a rheology (Mader et al., 2013). And we note that all experimental data analysed here are restricted to $\phi < 0.33$ and therefore to apply this approach to the multiphase scaling for magma failure requires additional validation or adjustment for high-ϕ, where Eq. (3) is insufficient. This shortcoming is mitigated by the observation that most dome lavas fall in this same range of low-ϕ (Mueller et al., 2005). Despite these shortcomings, we find excellent agreement between the compiled dataset and the viscous-brittle transition defined by $\mathrm{Wi}(\phi_x, \phi)$ proposed here (Figs. 8 and 9). This suggests that our simplistic micro-mechanical scaling holds at laboratory conditions.

6. Upscaling: constraining the regimes of lava dome advance

The analysis we have presented here shows that by scaling for the concentration of shear stress (or equivalently, strain rate) in the melt around suspended crystals and the gas phase, we can find a scaling for the transition from viscous flow to micro-fracturing in multiphase magmas on the sample scale. Further, we have used a simple approach to empirically extend this to account for a suspended gas phase; an approach that is probably restricted to low-ϕ (but still within the range of porosity of dome lavas). This apparent multiphase description of the flow transition performs well across all available experimental data where brittle or viscous outcomes were reported (Fig. 8). Next, we can apply this to the conditions of the shallowest portion of lava dome ascent and subsequent emplacement, in order to test whether lava domes are emplaced by dominantly viscous or micro-fracturing processes in nature. In order to compute Wi', we must find values for η and $\dot{\gamma}$ for natural scenarios.

First, we scale for the viscosity η for dome-forming magmas. Taking the composition of interstitial glass, and estimates for eruption temperature T and melt water concentration at eruption C, we can use a Newtonian viscosity compositional model (Giordano et al., 2008) for rhyolitic liquid viscosity $\mu = f(T, C)$. To find η, we then take a simple model for the effect of crystals on the suspension viscosity $\eta = \mu\left(1 - \phi'_x/\phi_m\right)^{-2}$, after Maron and Pierce (1956). This model underpins one of the most widely
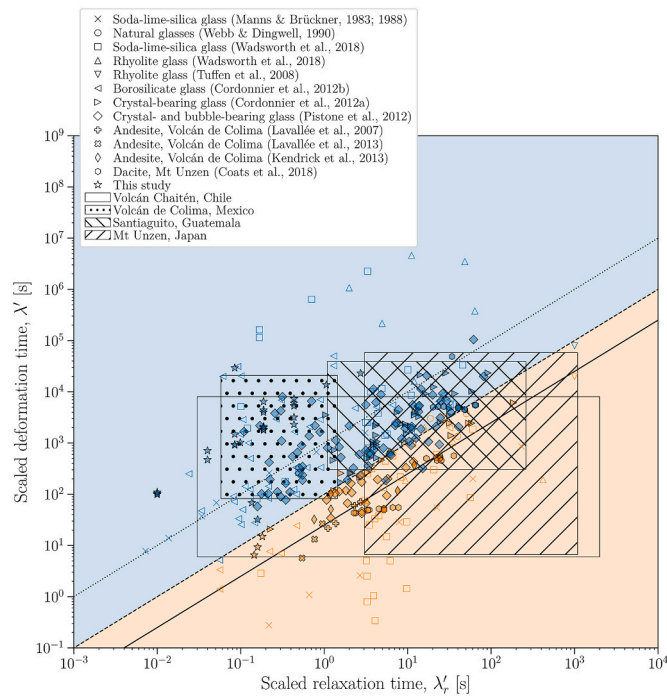
Fig. 9. A viscoelastic scaling map for the micromechanics of dome lava response to applied stress. The deformation timescale is $\lambda = 1/\dot{\gamma}$ (for single-phase melts), $\lambda' = 1/\dot{\gamma}'$ (for multiphase magmas), and the relaxation timescale is $\lambda_r' = \eta/G$. The proposed critical value of Wi = 0.01 is shown, along with Wi = 0.001 and Wi = 0.04, thought to be the onset of micro-brittleness and complete sample failure, respectively (Wadsworth et al., 2018; Vasseur et al., 2023). Data for single-phase melts are shown as un-filled points or crosses (Manns and Brückner, 1983, 1988; Webb and Dingwell, 1990; Tuffen et al., 2008; Cordonnier et al., 2012b; Wadsworth et al., 2018). Data for multiphase magmas are shown as filled points and are from this study, as well as published sources (Lavallée et al., 2007, 2013; Pistone et al., 2012; Cordonnier et al., 2012a; Kendrick et al., 2013; Coats et al., 2018). The scaled dome emplacement conditions are shown as boxes, the edges to which denote the minimum and maximum possible values of λ' and λ_r'. The conditions used to scale both the experimental data and the natural data are given in Table 3.

used crystal-bearing magma viscosity models (Mader et al., 2013). In Table 3, we give a compilation of the inputs to this approach for η for dome-forming magmas worldwide. Accounting for gas volume fraction can additionally be achieved by assuming either high or low capillarity after Mader et al. (2013) and the effective medium approach outlined by Truby et al. (2015). However, we note that at the typically low gas volume fractions of dome lavas ($\phi \leq 0.35$) this contribution is minor in the present case. Therefore, we neglect gas volume fraction from the estimate of η.

Second, we must scale for the strain rates characteristic of lava dome eruptions. By making the simplifying assumption of Poiseuille flow in the shallow conduit, we can find the mean strain rate across a rising flowing magma $\langle\dot{\gamma}\rangle = 8Q/(3\pi R^3)$, where Q is the volume flux and R is the conduit radius. By applying our scaling for the effect of crystals and bubbles on the local strain rate in the melt (e.g. Eq. (3)), we find that $\langle\dot{\gamma}\rangle' = 8Q/\left[3\pi R^3\left(1 - \phi_x'/\phi_m\right)\right]$ (or the porous variant thereof). These scaled strain rates are conservative estimates given that (1) the maximum strain rate at the conduit margin will be higher than the average strain rate by a factor of four (Gonnermann and Manga, 2003), and (2) there is prodigious field evidence for flow and strain localisation, such that some regions of emplacing domes may experience non-Poiseuille flow and locally higher strain rates (e.g., Wallace et al., 2019). In Table 3, we give collated observational constraints of Q and R for dome-forming eruptions worldwide. Where Q is not known, we provide published estimates of an average magma ascent velocity $\langle u\rangle$ and take $\langle\dot{\gamma}\rangle = 8\langle u\rangle/(3R)$.

Using the constraints provided in Table 3, we can place bounds on both λ_r' and λ', and therefore on Wi'. In Fig. 7, we show a general regime map for lava dome emplacement with examples from the 2008 eruption of Volcán Chaitén (Chile), eruptions of Volcán de Colima, eruptions of Santiaguito dome, and the 1995–97 eruption of Mt Unzen (Fig. 2). In all cases, we look for the maximum and minimum values of λ_r and λ' to bracket the range of Wi' for the range of conditions and magma properties (Table 3). We find that, for the dome lavas considered here, the lower and upper bounds on Wi' straddle Wi'$_c$ (Fig. 9). Given that our upper bounds on Wi' are based on conservative strain rate estimates, we propose that dome lavas typically can experience a micro-fracturing component to their flow mechanics during emplacement, contrary to many existing models that assume purely viscous behaviour. Furthermore, we note that our experimental results cover a range of Wi' similar

Table 3
Data used to scale natural observations at dome forming eruptions.

Volcano	Groundmass dissolved water concentration at emplacement, C	Crystallinity (dense rock equivalent; DRE), ϕ_x'	Crystal maximum packing, ϕ_m	Emplacement temperature estimate, T	Estimated conduit radius, R	Eruption volume flux, Q	Estimated magma ascent rate, u	References
	wt.%	–	–	°C	m	m³·s⁻¹	m·s⁻¹	
Volcán Chaitén	0.15–0.4	0	–	825	5	–	0.1–0.5	(Castro and Dingwell, 2009; Castro et al., 2012; Wadsworth et al., 2018)
Volcán de Colima	Nominally dry	0.5–0.7	0.75	959	12–15	0.17–4.4	–	(Luhr, 2002; Lavallée et al., 2007; Reubi et al., 2013; Kendrick et al., 2013)
Unzen volcano 1995–97	0.12–0.18	0.4–0.58	0.75	780–880	3.5–25	2.3–4.6	0.0002–0.0039	(Nakada and Motomura, 1999; Goto, 1999; Nakada et al., 2005; Lavallée et al., 2007; Noguchi et al., 2008; Cordonnier et al., 2009; Coats et al., 2018; Goto et al., 2020)
Santiaguito dome	Nominally dry	0.35–0.47	0.75	750–850	18	0.25–0.37	–	(Sahetapy-Engel et al., 2004; Holland et al., 2011; Scott et al., 2012)
Mt St Helens 2004–08	Nominally dry	High crystallinity (see Fig. 9)	Unknown or n/a (see Fig. 9)	700–850	25–50	–	0.000127	(Pallister et al., 2008; Smith et al., 2011)

to that estimated above for lava dome emplacement (Fig. 9).

We conclude that micro-fracturing may be characteristic of dome emplacement yet need not necessarily manifest itself in macroscopic lava failure, being accommodated instead by distributed damage processes at the microstructural scale. It is interesting to note that broadly similar deformation modes are observed at low temperatures in sandstones in the ductile regime, where local cataclasis leads to apparent flow even thought the process is microscopically brittle (Wong et al., 1997). From our permeability determinations on our experimental samples (Fig. 6), it is clear that mixed viscous-fracturing lava dome emplacement has consequences for the development of permeability anisotropy, with permeability maximum approximately perpendicular to the principal shear stress, potentially promoting distributed outgassing networks in domes.

7. Discussion

Our scaling for the conditions under which lava dome eruption and advance may be accompanied by distributed damage extends existing approaches that account for microstructural damage during flow of single-phase magmatic liquids (Tuffen et al., 2008; Cordonnier et al., 2012b; Wadsworth et al., 2018) to multiphase magmas (Lavallée et al., 2007, 2013; Pistone et al., 2012; Cordonnier et al., 2012a; Kendrick et al., 2013; Coats et al., 2018). Those existing scaling results via Wi have been used to suggest that degassed crystal-poor lava domes, such as the 2008 Volcán Chaitén dome, are emplaced with a flow mechanism that includes micro-cracking (Wadsworth et al., 2018) (see Fig. 9). Here, we have shown that multi-phase dome magmas may also typically advance by a combination of viscous flow and mixed viscous-fracturing flow, generalising the previous result. Direct evidence for this has been found in the study of dome lava textures (e.g., Goto, 1999; Kendrick et al., 2017; Lavallée et al., 2022) so that our quantitative predictions of dome emplacement regimes are consistent with natural observations. Our results, together with these previous observations, may explain (1) the recent recognition that laboratory-based viscosity values for Mt. Unzen lavas do not match viscosities estimated from lava dome extrusion rates when a purely viscous mechanism is assumed (Goto et al., 2020), (2) the widespread evidence of lava domes hosting opening and closing fractures that are sufficiently through-going to tap gas sources within the conduit core (Goto, 1999; Holland et al., 2011; Zorn et al., 2020), and (3) textural evidence for fractures on a variety of scales internal to dome lavas that are variably healed while still hot (Castro et al., 2012; Kolzenburg et al., 2012; Kendrick et al., 2016; Wallace et al., 2019; Lavallée et al., 2022). Our work additionally maps the conditions required for permeability anisotropy induced by directional fracturing (Fig. 4).

7.1. Previous experiments do not disambiguate flow from fracture

Much of the experimental work re-analysed herein aimed specifically to document whether samples deformed in a viscous or a brittle manner (Pistone et al., 2015; Coats et al., 2018). However, other work on the deformation of dome lavas or crystal-bearing magmas in general has aimed to find simple relationships for the temperature- and strain-rate dependence of the viscosity (Lejeune and Richet, 1995; Caricchi et al., 2007; Lavallée et al., 2007; Avard and Whittington, 2012; Kendrick et al., 2013) without necessarily dwelling on whether or not the experiments were in the brittle or the viscous field. Using our framework (Eqs. (1)–(4); Fig. 9), we can estimate both λ' and λ'_r for studies that aim to provide dome lava viscosity. In Fig. 10 we show where rheology experiments from published sources would plot in our deformation field. This analysis shows that there is inconsistency in the extent to which existing rheological work is capturing purely viscous flow (such as in the case of Avard and Whittington, 2012) or dominantly mixed viscous-
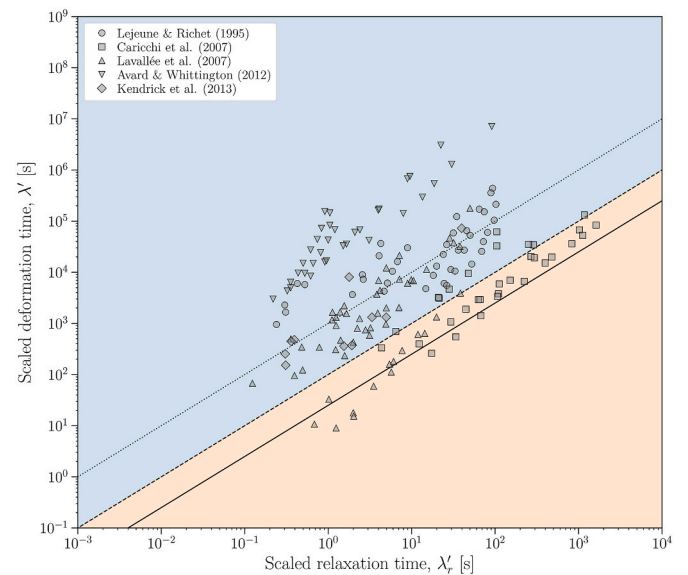

Fig. 10. Where do existing rheological experiments using dome lavas sit in the deformation map proposed here? This shows that while some experiments are exclusively in the viscous field (Avard and Whittington, 2012) some studies straddle the viscous and brittle fields (Caricchi et al., 2007; Lavallée et al., 2007) making the associated viscosity laws appropriate only for mixed-mode flow.

brittle flow (such as in the case of Caricchi et al., 2007; Lavallée et al., 2007). And yet, the empirical rheological flow laws that are proposed by these authors are inter-compared as if they are mapping the same deformation modes (Avard and Whittington, 2012). In future, the purely viscous flow data should be compared with multiphase viscosity models (Truby et al., 2015) and the mixed viscous-brittle flow data should be treated separately. The flow laws that result from those mixed viscous-brittle flow data probably represent an approximate flow law specifically for damaged lava at an intermediate Weissenberg number.

7.2. Macroscopic flow accommodated by micro-cracking

Our approach to upscaling our compilation of dome lava rheological measurements (Lavallée et al., 2007, 2013; Smith et al., 2011; Pistone et al., 2012; Cordonnier et al., 2012a; Kendrick et al., 2013; Coats et al., 2018) to the conditions of dome emplacement by using strain rates predicted by Poiseuille's law (Fig. 9) may be a simplistic one. Once dome lava has left the conduit, it undergoes a complex switch to lateral spreading onto the volcano surface (see Fig. 1 for examples), which has the potential to re-distribute strain and the local rate of strain (Adam et al., 2024) in a way not captured by our scaling. Model results show that localisation of strain over large scales occurs when the dome's internal pressures are large or when the extrusion occurs in a preferred direction, for example due to solidification of earlier magma preventing equal surface flow in all directions (Harnett et al., 2018).

Localisation of high strain at conduit margins due to non-Poiseuille flow and a shift toward plug-like flow is a central prediction of existing models of dome lava ascent (Gonnermann and Manga, 2003). We note that this increases the strain rate locally and renders it more likely that shallow magma ascent could be accompanied by brittleness at conduit margins. A full model of dome lava emplacement would require that the rheology of the internally fractured, but not failed, magma is modelled separately from purely viscous lava, such that at a local $Wi' < Wi'_c$, a multiphase suspension viscosity (without fractures) is used (Mueller et al., 2011) and at $Wi' > Wi'_c$, a model for multiphase viscosity that incorporates dynamic fracture-healing processes is used (Lavallée et al., 2007).
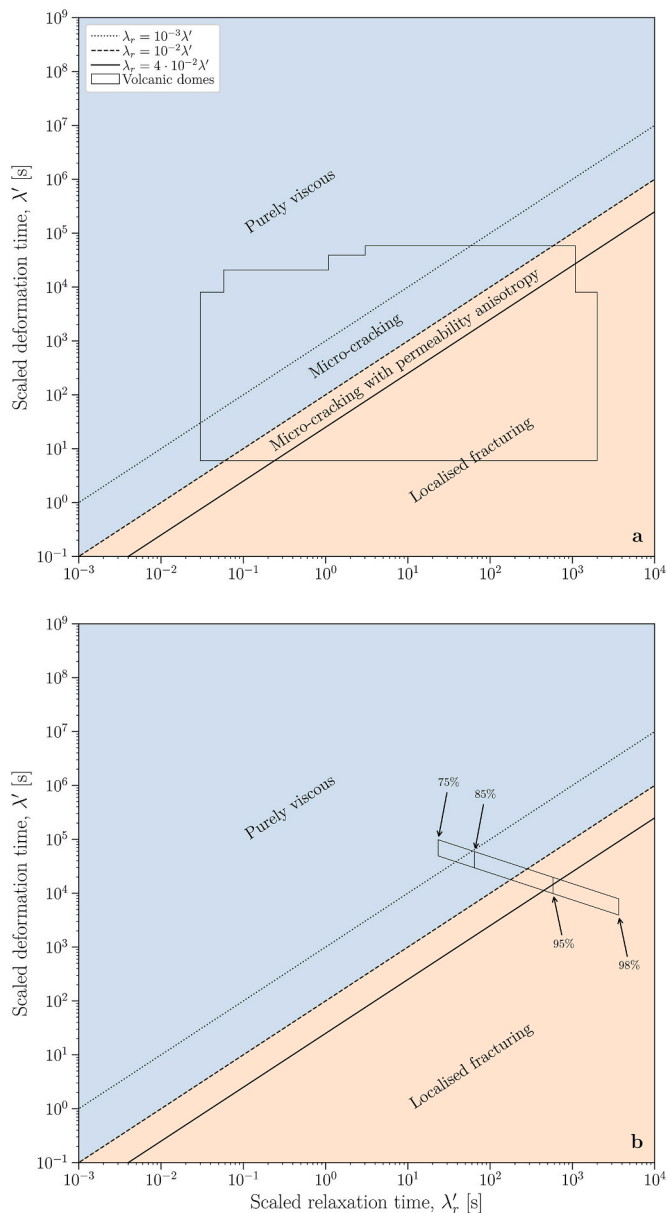
Fig. 11. Interpretations and points of discussion associated with the deformation map. (a) A stripped-down version of Fig. 9, but with the micro-mechanical interpretation of the dynamic fields labelled. (b) An example of applying our scaling to the condition $\phi'_x \rightarrow \phi_m$ using the conditions of emplacement for the 2004–08 dome at Mt. St Helens (U.S.A.; Table 3) shown for values of ϕ'_x/ϕ_m of 0.75, 0.85, 0.9 and 0.98 (on the plot the crystallinity is given as a percentage of the brittle field at very high crystallinities. Note that in reality the 2004–08 dome at Mt. St Helens was emplaced in a near fully crystallized state such that $\phi'_x > \phi_m$ and this scaling is invalid.

7.3. Limitations and the use of a 'maximum packing' of crystals

When performing upscaling such as given here, it is important to consider limitations to these relatively simple approaches. We consider that a primary limitation to our approach is well-illustrated by the observations of the 2004–2008 eruption of Mt. St Helens. Specifically, while some glass-dominated dacite was found in the earliest erupted material from November 2004, the majority of the erupted material was very high crystallinity and perhaps even fully crystalline with no glass present (Pallister et al., 2008; Smith et al., 2011). Given that our scaling

relies on a ratio between the crystallinity and a maximum packing of crystals (Eqs. (3) and (4)), it simply cannot predict the rheological behaviour of very highly crystalline materials. The concept of ϕ_m relies on packing of existing crystals into a framework (surrounded by melt and pores) but does not account for in-situ crystal growth that can infill this framework at the expense of the melt phase, apparently raising crystallinity above ϕ_m. To illustrate the issue here, we use the known emplacement conditions of the 2004–2008 eruption of Mt. St Helens in terms of inferred conduit radius and ascent rate (Table 3; Pallister et al., 2008; Smith et al., 2011). Then we show that as the ratio of ϕ'_x/ϕ_m increases from values of 0.75 to 0.98, the predicted regime in which the dome lava emplacement sits migrates from mixed viscous-brittle to purely brittle (Fig. 11). Because the change in rheology predicted by Eqs. (3) and (4) evolves sharply as $\phi'_x \rightarrow \phi_m$ (see Fig. 4), this shift in predicted behaviour type is dramatic as ϕ_m is approached. While anything more crystalline than ϕ_m cannot explicitly be captured by this analysis, it is reasonable that such high-crystallinity materials would be wholly brittle in terms of micro-mechanical deformation mechanisms when subjected to stress. Therefore, the emplacement of the 2004–2008 dome lava at Mt. St Helens is predicted to be purely brittle in terms of micro-mechanisms, which is consistent with previous work which documents the brittle nature of many of the features of dome and spine emplacement during this eruption (Pallister et al., 2008; Smith et al., 2011; Gaunt et al., 2014). Fundamentally, the utility and appropriateness of any model that relies on ϕ_m may be questioned when it comes to very high crystallinity materials and future experiments on solid, fully crystalline volcanic materials could be useful in developing rheological models for the space $\phi'_x > \phi_m$.

7.4. Micro-mechanisms for permeability anisotropy development

In our experiments, at high relative strain rates, we find that the permeability in the x and y directions (perpendicular to the direction of compression in our rheometry tests) is substantially different from the permeability in the z direction parallel to the compression (Fig. 6). In our experiments, we find that it is the direction perpendicular to the direction of compression that ends up being the direction in which the permeability is largest, whereas the direction parallel to compression is the direction in which there is a form of compaction-related permeability reduction. It is important to interpret this, especially in light of previous work that suggests that shear-induced fracturing produces high/elevated permeability parallel to the flow direction (Okumura et al., 2008; Caricchi et al., 2011).

Our experiments involve the compression of a viscous cylinder of magma in one direction. This is known to produce a spatially heterogeneous shear stress environment (Gent, 1960) such that our application of the Trouton rule to correct the compressive stress to the shear stress is an approximation. That approximation appears to be sufficient to extract a bulk average shear stress that is useful for scaling the viscous-brittle transition (Wadsworth et al., 2018) but may be insufficient for understanding what are inherently local processes like intra-sample fracture network development and associated permeability anisotropy. Knowing that the bulk stress applied to our cylinders is uniaxial, and knowing that the fracturing process is mechanistically linked to an elastic response of the melt in a viscoelastic medium (Dingwell and Webb, 1989; Webb and Dingwell, 1990; Vasseur et al., 2023), we can use elasticity theory to better understand the stress response locally. In the elastic limit and under uniaxial compression conditions, inclusions such as pores or crystals concentrate stress around them. The poles that are aligned with the uniaxial compression direction produce compressive stress concentration, whereas the edges of the pore or crystal that are perpendicular to that uniaxial compression direction produce tensile stress concentrations (Sammis and Ashby, 1986; Vasseur et al., 2017). If we assume that the inclusion in question is a crystal and that the groundmass around it is porous (Fig. 3) then it is likely that the

permeable-porous groundmass material would compact where the stresses are compressive (in polar compression fields parallel with the uniaxial compression direction) and would rupture in the tensile directions, if that tensile stress meets the Weissenberg number limit proposed here. This interpretation is then consistent with our permeability determinations which show that it is those poles perpendicular to the uniaxial compression direction that produce micro-fractures associated with the permeability increase. Furthermore, this suggests that the micro-mechanism for permeability increase is the coalescence of small micro-fractures in a preferred orientation in such a way as to increase the efficiency of gas-flow in that direction, but not sufficient to produce macroscopic failure.

If the interpretation given above is correct, then it suggests that our results for permeability anisotropy may be specific to the uniaxial compression test geometry. While it is tempting to think that in uniaxial compression, we are forcing the magma to flow in the direction parallel to the maximum compressive stress, the reality is that the stress and strain fields are complex in our tests. To understand the orientation of permeability anisotropy in response to rupture during flow, one should focus on experiments for which the strain was viscometric or simple-shear (Okumura et al., 2008; Kushnir et al., 2017a). Nevertheless, what we do confidently learn from our tests is (a) that there is a bulk Weissenberg number window for which micro-cracking occurs but for which system-spanning rupture does not, and (b) that where the conditions for micro-cracking are met, the resultant permeability can be anisotropic (note that if the confining pressures are appreciable, these fractures may close). Because we have scaled for the bulk Weissenberg number in our analysis, this interpretation is likely to be geometry independent. In simple-shear, inclusions such as pores and crystals still create anisotropic stress concentrations, and so similar anisotropic micro-crack and permeability development are likely to result.

7.5. Spatial variations in Weissenberg number and localized fracturing

The first criterion proposed here for the transition from purely viscous flow to mixed flow-and-fracture in melt suspensions of crystals and pores, is a local criterion. In our upscaling to dome magma emplacement, we have simply asked the question if the average shear stress during conduit flow will hit that criterion for a transition to mixed flow-and-fracture. Given that most dome emplacement conditions do meet that criterion, then we propose here that magmas feeding dome emplacement are not just forming large-scale through-going fractures at the high strain-rate conduit margins (Gonnermann and Manga, 2003; Holland et al., 2011; Lavallée et al., 2013) but also that the magma is, on a smaller scale, fracturing as it "flows" during emplacement. Put another way: dome emplacement involves distributed fracturing at the scale of crystals and pores and this has implications for magma permeability even away from larger fractures. The second criterion for the transition from mixed flow-and-fracture to localized fracturing (see Fig. 11) is system-spanning and involves the development of through-going fractures. This kind of fracturing is more akin to the large conduit-margin fractures proposed previously (Lavallée et al., 2013; Kushnir et al., 2017a) and given that the strain rates are highest at those conduit margins, it is likely that these kinds of larger fractures will form there first.

Our upscaling has focussed on simple considerations of upper conduit flow. However, magmas feeding domes can produce complex intra-dome flow and strain distributions (Harnett et al., 2018). Simply to illustrate this, we reproduce published results (Harnett et al., 2018; Walter et al., 2019) from discrete element models converted to local strain rate (i.e. linear related to Weissenberg number) in order to demonstrate qualitatively that internal to dome lavas there can be a spatially heterogeneous local Weissenberg number. While these models are strictly 2D – and therefore we do not attempt to quantitatively map Weissenberg number – they give the clear indication that high and low Weissenberg number patterns can be spatially heterogeneous, opening up the possibility that fracturing in domes can sometimes be spatially distributed (Fig. 12a–12d), or localized close to the dome carapace (Fig. 12e–h), or in endogenous spine-like features (Fig. 12i–l) depending on the driving mass eruption rates, and/or the local solidification patterns in the dome (Harnett et al., 2018). In future, our local fracturing criterion should be embedded in simulations such as these.
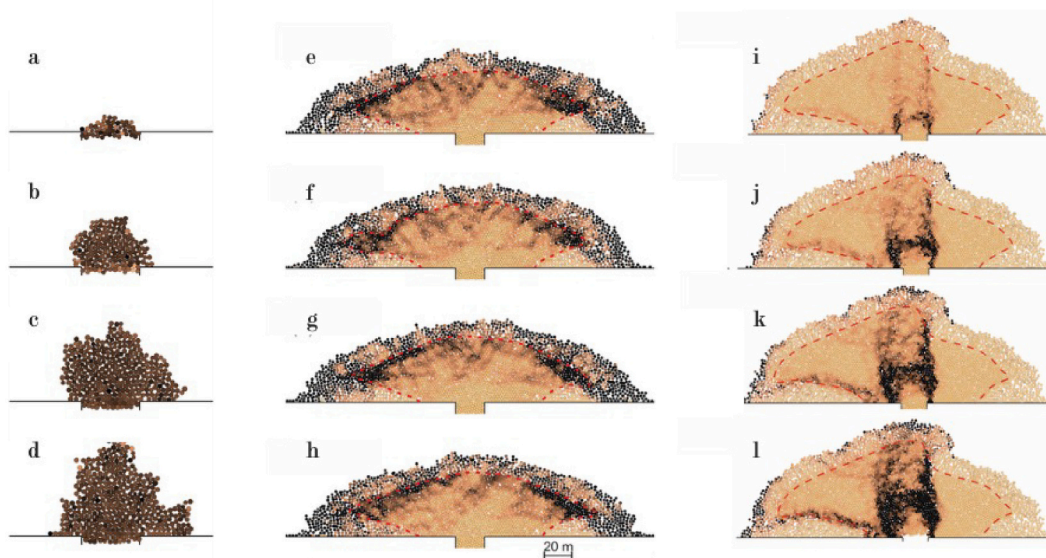

Fig. 12. (a-d) Discrete element models showing scaled deformation time λ_d of particles in the dome core, calculated from shear strain rate in the time-calibrated model presented in Walter et al. (2019); (e-f) Existing discrete element models showing normalized finite shear strain following application of an upward force corresponding to (e) 0 MPa, (f) 1 MPa, (g) 2 MPa, (h) 5 MPa. Red dotted line shows interface between dome core and talus; (i-l) Existing discrete element models showing normalized finite shear strain following forced solidification of the right hand side of the dome. Models show snapshots of increasing runtime, where red dotted line shows core/talus interface. Panels e-l taken from Harnett et al. (2018), and all models performed using Particle Flow Code 2D from Itasca Consulting Group. Note that no colour bar scale is given because the results are simply meant to qualitatively show where regions of high λ_d (orange) and low λ_d (black) occur. (For interpretation of the references to colour in this figure legend, the reader is referred to the web version of this article.)

8. Conclusions

Previous work has shown that magma can be emplaced with a brittle component to the bulk deformation. In general, this is thought to be associated with moderate- to large-scale deformation features such as a heavily fractured conduit margin and associated annulus of damaged magma. We have demonstrated experimentally that this behaviour is associated with high Weissenberg number conditions – such that the magma is being deformed at a rate comparable to or larger than the rate of viscoelastic relaxation of the multiphase mixture. Put another way: magma will produce large system-spanning fractures associated with bulk failure at high Weissenberg number. This kind of behaviour is clearly associated with permeability anisotropy where the large system-spanning fractures will be sub-parallel to the direction of flow, providing connected vertical outgassing pathways (see Fig. 13a). In addition to the behaviour described above, previous work has also shown that at the other end of the spectrum of deformation rate, the behaviour will be purely viscous. That is, magma will flow without any fracturing occurring at any scale. We show experimentally that this is associated with low bulk Weissenberg number $Wi' \leq 0.01$, when the Weissenberg number is adjusted to account for the effect of crystals and pore space. The prevailing view of silicic magma ascent, outgassing, and dome emplacement, holds that the centre of volcanic conduits tends to be viscous and not brittle, and that the margins host brittle behaviour.

In this contribution, we show experimentally that there is a mixed regime between the two end-members described above. That is, that magma appears to flow on the sample (or larger) scale but, on the micro-scale, strain is accommodated by micro-cracking and the coalescence of micro-cracks, connecting neighbouring microstructural elements such as crystals or pores. But, importantly, that the magma remains coherent so that no single macroscopic fracture forms. We analyze this regime and find that it occurs in a defined window of bulk Weissenberg number $0.01 \leq Wi' \leq 0.04$, in which the magma remains a continuum, but hosting micro-cracks. By reanalyzing the large body of existing work on the rheology of silicic multiphase magmas, we show that many experiments sit in or straddle this regime, potentially explaining why rheological laws differ from study-to-study. Our explanation for this is simply that some experiments are describing the continuum flow behaviour of fractured magma, while others are describing the continuum flow behaviour of non-fractured magma. We propose that attempts at unification of rheological regimes should separate out these regimes and that there is a clear need for a rheological law that can account for the flow of partially damaged magma.

Finally, by looking at the magma ascent and dome emplacement conditions of dome-forming eruptions worldwide, we find that dome emplacement straddles all three regimes: viscous, brittle, and mixed viscous-brittle. This hammers home the need for rheological models for both the viscous (suspension rheology) and the mixed viscous-brittle (complex rheology) regimes. The fact that many domes could accommodate some mixed viscous-brittle flow leads us to suggest that there
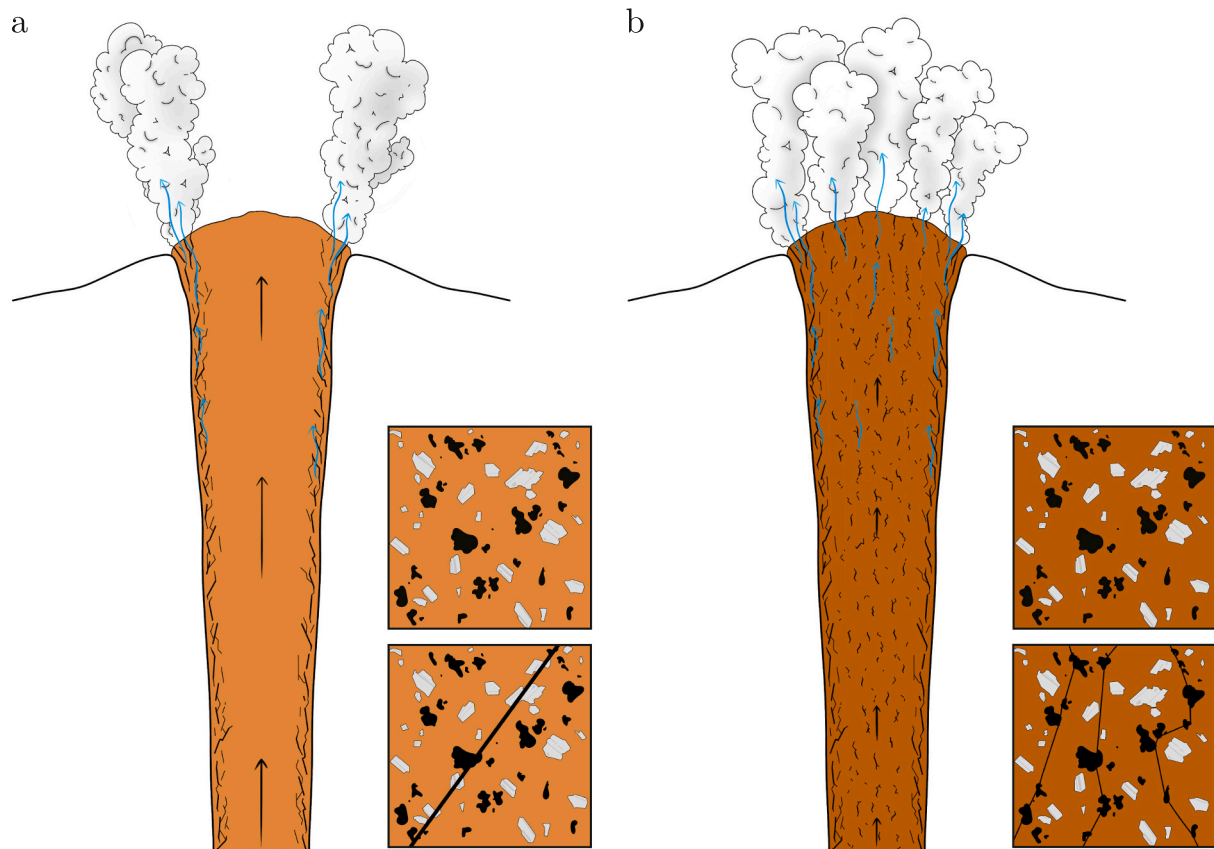

Fig. 13. Cartoon portrayals of magma ascent feeding surface dome emplacement. (a) The existing conceptual model in which magma ascent undergoes brittle fracturing at the conduit margins forming a damaged permeable conduit annulus (.g. Gonnermann and Manga, 2003). (b) The possibility raised in this study: that magma can be mixed brittle-viscous without wholesale failure, such that damage is pervasive and distributed throughout the magma, if the local Weissenberg number environment is sufficient for a partly brittle response to stress (see Fig. 9). *Insets*: the micromechanics invoked to interpret these two regimes showing (a) the localized fracture development and (b) the distributed and not necessarily through-going fracture development. Note that the magma in (b) is depicted a different colour from (a) to acknowledge the potential for compositional and temperature controls on the regime of ascent. Large-scale connected conduit margin fracturing (as in (a)) can still occur in the regime depicted in (b).

could be ascent conditions – in terms of Wi′ - for which the conduit will be pervasively damaged, but not strictly fractured in the large-scale sense. In this commonly-observed mixed regime, the resultant permeability structure is anisotropic, but complex, and presumably leads to more pervasive and spatially thorough outgassing (see Fig. 13b). The outgassing associated with magmas that are emplaced in a mixed brittle-viscous regime may be sufficient to bleed gas pressure and have a control on gas pressure build-up, potentially with implications for the propensity for subsequent returns/transitions to explosive behaviour.

Author contributions

F.B. Wadsworth, M.J. Heap, J. Vasseur, and D.B. Dingwell conceived the laboratory project. F.B. Wadsworth, J. Vasseur, and D. Weller conducted the deformation experiments and analysed the data with L. Pereira and Y. Lavallée, J.E. Kendrick, A. Lamur, and C. Harnett. All authors contributed to the manuscript.

CRediT authorship contribution statement

Fabian B. Wadsworth: Writing – review & editing, Writing – original draft, Visualization, Formal analysis, Conceptualization. **Jérémie Vasseur:** Writing – review & editing, Formal analysis, Conceptualization. **Michael J. Heap:** Writing – review & editing, Data curation, Conceptualization. **Jackie E. Kendrick:** Writing – review & editing. **Claire E. Harnett:** Writing – review & editing, Formal analysis, Conceptualization. **Annabelle Foster:** Visualization. **Daniel Weller:** Writing – review & editing, Formal analysis. **Bettina Scheu:** Writing – review & editing, Formal analysis, Conceptualization. **Anthony Lamur:** Writing – review & editing. **Luiz Pereira:** Writing – review & editing. **Donald B. Dingwell:** Writing – review & editing, Resources, Funding acquisition. **Yan Lavallée:** Writing – review & editing.

Declaration of competing interest

The authors declare that they have no known competing financial interests or personal relationships that could have appeared to influence the work reported in this paper.

Data availability

All data is provided with this manuscript.

Acknowledgments

Appendix A. Supplementary data

Supplementary data to this article can be found online at https://doi.org/10.1016/j.jvolgeores.2024.108198.

References

Adam, S., Sparks, R.S.J., Huppert, H.E., 2024. Analysis of magma rheology from lava spreading and explosive activity during the 2020–21 eruption of La Soufrière, St Vincent, with implications for eruption dynamics. Geol. Soc. Lond., Spec. Publ. 539, 153–169. https://doi.org/10.1144/SP539-2022-284.

Andrews, G.D.M., Kenderes, S.M., Whittington, A.G., Isom, S.L., Brown, S.R., Pettus, H. D., Cole, B.G., Gokey, K.J., 2021. The fold illusion: the origins and implications of ogives on silicic lavas. Earth Planet. Sci. Lett. 553, 116643. https://doi.org/10.1016/j.epsl.2020.116643.

Ashwell, P.A., Kendrick, J.E., Lavallée, Y., Kennedy, B.M., Hess, K.U., Von Aulock, F.W., Wadsworth, F.B., Vasseur, J., Dingwell, D.B., 2015. Permeability of compacting porous lavas. J. Geophys. Res. Solid Earth 120, 1605–1622. https://doi.org/10.1002/2014JB011519.

Avard, G., Whittington, A.G., 2012. Rheology of arc dacite lavas: experimental determination at low strain rates. Bull. Volcanol. 74, 1039–1056. https://doi.org/10.1007/s00445-012-0584-2.

Birnbaum, J., Lev, E., Llewellin, E.W., 2021. Rheology of three-phase suspensions determined via dam-break experiments. Proc. Roy. Soc. A Math. Phys. Eng. Sci. 477, 20210394. https://doi.org/10.1098/rspa.2021.0394.

Calder, E.S., Lavallée, Y., Kendrick, J.E., Bernstein, M., 2015. Lava Dome eruptions. In: The Encyclopedia of Volcanoes. Elsevier, pp. 343–362. https://doi.org/10.1016/b978-0-12-385938-9.00018-3.

Caricchi, L., Burlini, L., Ulmer, P., Gerya, T., Vassalli, M., Papale, P., 2007. Non-Newtonian rheology of crystal-bearing magmas and implications for magma ascent dynamics. Earth Planet. Sci. Lett. 264, 402–419. https://doi.org/10.1016/j.epsl.2007.09.032.

Caricchi, L., Pommier, A., Pistone, M., Castro, J., Burgisser, A., Perugini, D., 2011. Strain-induced magma degassing: insights from simple-shear experiments on bubble bearing melts. Bull. Volcanol. 73, 1245–1257. https://doi.org/10.1007/s00445-011-0471-2.

Castro, J.M., Dingwell, D.B., 2009. Rapid ascent of rhyolitic magma at Chaitén volcano, Chile. Nature 461, 780–783. https://doi.org/10.1038/nature08458.

Castro, J.M., Cordonnier, B., Tuffen, H., Tobin, M.J., Puskar, L., Martin, M.C., Bechtel, H. A., 2012. The role of melt-fracture degassing in defusing explosive rhyolite eruptions at volcán Chaitén. Earth Planet. Sci. Lett. 333–334, 63–69. https://doi.org/10.1016/j.epsl.2012.04.024.

Coats, R., Kendrick, J.E., Wallace, P.A., Miwa, T., Hornby, A.J., Ashworth, J.D., Matsushima, T., Lavallée, Y., 2018. Failure criteria for porous dome rocks and lavas: a study of Mt. Unzen, Japan. Solid Earth 9, 1299–1328. https://doi.org/10.5194/se-9-1299-2018.

Colombier, M., Wadsworth, F.B., Gurioli, L., Scheu, B., Kueppers, U., Di Muro, A., Dingwell, D.B., 2017. The Evolution of Pore Connectivity in Volcanic Rocks, vol. 462. https://doi.org/10.1016/j.epsl.2017.01.011.

Cordonnier, B., Hess, K.-U., Lavallée, Y., Dingwell, D.B., 2009. Rheological properties of dome lavas: Case study of Unzen volcano. Earth Planet. Sci. Lett. 279, 263–272. https://doi.org/10.1016/j.epsl.2009.01.014.

Cordonnier, B., Caricchi, L., Pistone, M., Castro, J., Hess, K.U., Gottschaller, S., Manga, M., Dingwell, D.B., Burlini, L., 2012a. The viscous-brittle transition of crystal-bearing silicic melt: Direct observation of magma rupture and healing. Geology 40, 611–614. https://doi.org/10.1130/G3914.1.

Cordonnier, B., Schmalholz, S.M., Hess, K.U., Dingwell, D.B., 2012b. Viscous heating in silicate melts: an experimental and numerical comparison. J. Geophys. Res. Solid Earth 117, B02203. https://doi.org/10.1029/2010JB007982.

Costa, A., Caricchi, L., Bagdassarov, N., 2009. A model for the rheology of particle-bearing suspensions and partially molten rocks. Geochem. Geophys. Geosyst. 10. https://doi.org/10.1029/2008GC002138.

Deubelbeiss, Y., Kaus, B.J.P., Connolly, J.A.D., Caricchi, L., 2011. Potential causes for the non-Newtonian rheology of crystal-bearing magmas. Geochem. Geophys. Geosyst. v, 12.

Dingwell, D.B., Webb, S.L., 1989. Structural relaxation in silicate melts and non-Newtonian melt rheology in geologic processes. Phys. Chem. Miner. 16, 508–516.

Farquharson, J., Heap, M.J., Varley, N.R., Baud, P., Reuschlé, T., 2015. Permeability and porosity relationships of edifice-forming andesites: a combined field and laboratory study. J. Volcanol. Geotherm. Res. 297, 52–68. https://doi.org/10.1016/j.jvolgeores.2015.03.016.

Farquharson, J.I., Heap, M.J., Lavallée, Y., Varley, N.R., Baud, P., 2016. Evidence for the development of permeability anisotropy in lava domes and volcanic conduits. J. Volcanol. Geotherm. Res. 323, 163–185. https://doi.org/10.1016/j.jvolgeores.2016.05.007.

Gaunt, H.E., Sammonds, P.R., Meredith, P.G., Smith, R., Pallister, J.S., 2014. Pathways for degassing during the lava dome eruption of Mount St. Helens 2004–2008. Geology 42, 947–950. https://doi.org/10.1130/G35940.1.

Gent, A.N., 1960. Theory of the parallel plate viscometer. Br. J. Appl. Phys. 11, 85.

Giordano, D., Russell, J.K., Dingwell, D.B., 2008. Viscosity of magmatic liquids: a model. Earth Planet. Sci. Lett. 271, 123–134.

Gonnermann, H.M., Manga, M., 2003. Explosive volcanism may not be an inevitable consequence of magma fragmentation. Nature 426, 432–435.

Goto, A., 1999. A new model for volcanic earthquake at Unzen Volcano: melt rupture model. Geophys. Res. Lett. 26, 2541–2544. https://doi.org/10.1029/1999GL900569.

Goto, A., Fukui, K., Hiraga, T., Nishida, Y., Ishibashi, H., Matsushima, T., Miyamoto, T., Sasaki, O., 2020. Rigid migration of Unzen lava rather than flow. J. Volcanol. Geotherm. Res. 407, 107073. https://doi.org/10.1016/j.jvolgeores.2020.107073.

Griffiths, L., Heap, M.J., Lengliné, O., Baud, P., Schmittbuhl, J., Gilg, H.A., 2024. Thermal stressing of volcanic rock: microcracking and crack closure monitored through acoustic emission, ultrasonic velocity, and thermal expansion. J. Geophys. Res. Solid Earth 129. https://doi.org/10.1029/2023JB027766.

Harnett, C.E., Thomas, M.E., Purvance, M.D., Neuberg, J., 2018. Using a discrete element approach to model lava dome emplacement and collapse. J. Volcanol. Geotherm. Res. 359, 68–77. https://doi.org/10.1016/j.jvolgeores.2018.06.017.

Heap, M.J., Russell, J.K., Kennedy, L.A., 2016. Mechanical behaviour of dacite from Mount St. Helens (USA): a link between porosity and lava dome extrusion mechanism (dome or spine)? J. Volcanol. Geotherm. Res. 328, 159–177. https://doi.org/10.1016/j.jvolgeores.2016.10.015.

Heap, M.J., Kushnir, A.R.L., Gilg, H.A., Wadsworth, F.B., Reuschlé, T., Baud, P., 2017. Microstructural and petrophysical properties of the Permo-Triassic sandstones (Buntsandstein) from the Soultz-sous-Forêts geothermal site (France). Geotherm. Energy 5, 26. https://doi.org/10.1186/s40517-017-0085-9.

Heap, M.J., Troll, V.R., Kushnir, A.R.L., Gilg, H.A., Collinson, A.S.D., Deegan, F.M., Darmawan, H., Seraphine, N., Neuberg, J., Walter, T.R., 2019. Hydrothermal alteration of andesitic lava domes can lead to explosive volcanic behaviour. Nat. Commun. 10, 1–10. https://doi.org/10.1038/s41467-019-13102-8.

Hess, K.-U., Cordonnier, B., Lavallée, Y., Dingwell, D.B., 2007. High-load, high-temperature deformation apparatus for synthetic and natural silicate melts. Rev. Sci. Instrum. 78, 75102–75104. https://doi.org/10.1063/1.2751398.

Holland, A.S.P., Watson, I.M., Phillips, J.C., Caricchi, L., Dalton, M.P., 2011. Degassing processes during lava dome growth: Insights from Santiaguito lava dome, Guatemala. J. Volcanol. Geotherm. Res. 202, 153–166. https://doi.org/10.1016/j.jvolgeores.2011.02.004.

Hornby, A.J., Lavallée, Y., Kendrick, J.E., De Angelis, S., Lamur, A., Lamb, O.D., Rietbrock, A., Chigna, G., 2019. Brittle-Ductile Deformation and Tensile Rupture of Dome Lava during inflation at Santiaguito. J. Geophys. Res. Solid Earth 124, 10107–10131. https://doi.org/10.1029/2018JB017253.

Kendrick, J.E., Lavallée, Y., Hess, K.U., Heap, M.J., Gaunt, H.E., Meredith, P.G., Dingwell, D.B., 2013. Tracking the permeable porous network during strain-dependent magmatic flow. J. Volcanol. Geotherm. Res. 260, 117–126. https://doi.org/10.1016/j.jvolgeores.2013.05.012.

Kendrick, J.E., Lavallée, Y., Varley, N.R., Wadsworth, F.B., Lamb, O.D., Vasseur, J., 2016. Blowing off steam: Tuffisite formation as a regulator for lava dome eruptions. Front. Earth Sci. 4. https://doi.org/10.3389/feart.2016.00041.

Kendrick, J.E., Lavallée, Y., Mariani, E., Dingwell, D.B., Wheeler, J., Varley, N.R., 2017. Crystal plasticity as an indicator of the viscous-brittle transition in magmas. Nat. Commun. 8, 1926. https://doi.org/10.1038/s41467-017-01931-4.

Kendrick, J.E., Schaefer, L.N., Schauroth, J., Bell, A.F., Lamb, O.D., Lamur, A., Miwa, T., Coats, R., Lavallée, Y., Kennedy, B.M., 2021. Physical and mechanical rock properties of a heterogeneous volcano: the case of Mount Unzen, Japan. Solid Earth 12, 633–664. https://doi.org/10.5194/se-12-633-2021.

Kolzenburg, S., Heap, M.J., Lavallée, Y., Russell, J.K., Meredith, P.G., Dingwell, D.B., 2012. Strength and permeability recovery of tuffisite-bearing andesite. Solid Earth 3, 191–198. https://doi.org/10.5194/se-3-191-2012.

Kushnir, A.R.L., Martel, C., Champallier, R., Arbaret, L., 2017a. In situ confirmation of permeability development in shearing bubble-bearing melts and implications for volcanic outgassing. Earth Planet. Sci. Lett. 458, 315–326. https://doi.org/10.1016/j.epsl.2016.10.053.

Kushnir, A.R.L., Martel, C., Champallier, R., Wadsworth, F.B., 2017b. Permeability evolution in variably glassy basaltic andesites measured under magmatic conditions. Geophys. Res. Lett. 44, 10210–262271. https://doi.org/10.1002/2017GL074042.

Lamb, O.D., De Angelis, S., Umakoshi, K., Hornby, A.J., Kendrick, J.E., Lavallée, Y., 2015. Repetitive fracturing during spine extrusion at Unzen volcano, Japan. Solid Earth 6, 1277–1293. https://doi.org/10.5194/se-6-1277-2015.

Lavallée, Y., Kendrick, J.E., 2022. Strain Localization in Magmas. Rev. Mineral. Geochem. 87, 721–765. https://doi.org/10.2138/rmg.2022.87.15.

Lavallée, Y., Hess, K.-U., Cordonnier, B., Dingwell, D.B., 2007. Non-Newtonian rheological law for highly crystalline dome lavas. Geology 35, 843–846. https://doi.org/10.1130/g23594a.1.

Lavallée, Y., Meredith, P.G., Dingwell, D.B., Hess, K.-U., Wassermann, J., Cordonnier, B., Gerik, A., Kruhl, J.H., 2008. Seismogenic lavas and explosive eruption forecasting. Nature 453, 507–510. https://doi.org/10.1038/nature06980.

Lavallée, Y., Benson, P.M., Heap, M.J., Hess, K.U., Flaws, A., Schillinger, B., Meredith, P.G., Dingwell, D.B., 2013. Reconstructing magma failure and the degassing network of domebuilding eruptions. Geology 41, 515–518. https://doi.org/10.1130/G33948.1.

Lavallée, Y., et al., 2022. Transient conduit permeability controlled by a shift between compactant shear and dilatant rupture at Unzen volcano (Japan). Solid Earth 13, 875–900. https://doi.org/10.5194/se-13-875-2022.

Lejeune, A.-M., Richet, P., 1995. Rheology of crystal-bearing silicate melts: an experimental study at high viscosities. J. Geophys. Res. Solid Earth 100, 4215–4229. https://doi.org/10.1029/94JB02985.

Lockner, D., 1993. The role of acoustic emission in the study of rock fracture. Int. J. Rock Mech. Min. Sci. Geomech. Abstr. 30, 883–899. https://doi.org/10.1016/0148-9062(93)90041-B.

Luhr, J.F., 2002. Petrology and geochemistry of the 1991 and 1998-1999 lava flows from Volcán de Colima, México: implications for the end of the current eruptive cycle. J. Volcanol. Geotherm. Res. 117, 169–194. https://doi.org/10.1016/S0377-0273(02)00243-3.

Mader, H.M., Llewellin, E.W., Mueller, S.P., 2013. The rheology of two-phase magmas: a review and analysis. J. Volcanol. Geotherm. Res. 257, 135–158. https://doi.org/10.1016/j.jvolgeores.2013.02.014.

Manns, P., Brückner, R., 1983. Biegefestigkeit von Kalk-Natron-und Borosilicatglas von Raumtemperatur bis zur Littleton-Temperatur: Glastechnische Berichte.

Manns, P., Brückner, R., 1988. Non-Newtonian flow behaviour of a soda-lime silicate glass at high deformation rates. Glastech. Ber. 61, 46–56.

Maron, S., Pierce, P., 1956. Application of Ree-Eyring generalized flow theory to suspensions of spherical particles. J. Colloid Sci. 11, 80–95.

Matthews, S.J., Gardeweg, M.C., Sparks, R.S.J., 1997. The 1984 to 1996 cyclic activity of Lascar Volcano, northern Chile: cycles of dome growth, dome subsidence, degassing and explosive eruptions. Bull. Volcanol. 59, 72–82. https://doi.org/10.1007/s004450050176.

Melnik, O., Sparks, R., 1999. Nonlinear dynamics of lava dome extrusion. Nature 402, 37–41.

Mueller, S., Melnik, O., Spieler, O., Scheu, B., Dingwell, D.B., 2005. Permeability and degassing of dome lavas undergoing rapid decompression: an experimental determination. Bull. Volcanol. 67, 526–538. https://doi.org/10.1007/s00445-004-0392-4.

Mueller, S., Llewellin, E.W., Mader, H.M., 2011. The effect of particle shape on suspension viscosity and implications for magmatic flows. Geophys. Res. Lett. 38, L13316. https://doi.org/10.1029/2011GL047167.

Nakada, S., Motomura, Y., 1999. Petrology of the 1991–1995 eruption at Unzen: effusion pulsation and groundmass crystallization. J. Volcanol. Geotherm. Res. 89, 173–196. https://doi.org/10.1016/S0377-0273(98)00131-0.

Nakada, S., Uto, K., Sakuma, S., Eichelberger, J.C., Shimizu, H., 2005. Scientific results of Conduit Drilling in the Unzen Scientific Drilling Project (USDP). Sci. Drill. 1, 18–22. https://doi.org/10.5194/sd-1-18-2005.

Neuberg, J.W., Tuffen, H., Collier, L., Green, D., Powell, T., Dingwell, D., 2006. The trigger mechanism of low-frequency earthquakes on Montserrat. J. Volcanol. Geotherm. Res. 153, 37–50. https://doi.org/10.1016/j.jvolgeores.2005.08.008.

Noguchi, S., Toramaru, A., Nakada, S., 2008. Groundmass crystallization in dacite dykes taken in Unzen Scientific Drilling Project (USDP-4). J. Volcanol. Geotherm. Res. 175, 71–81. https://doi.org/10.1016/j.jvolgeores.2008.03.037.

Okumura, S., Nakamura, M., Tsuchiyama, A., Nakano, T., Uesugi, K., 2008. Evolution of bubble microstructure in sheared rhyolite: formation of a channel-like bubble network. J. Geophys. Res. Solid Earth 113. https://doi.org/10.1029/2007JB005362.

Pallister, J.S., Thornber, C.R., Cashman, K.V., Clynne, M.A., Lowers, H., Mandeville, C. W., Brownfield, I.K., Meeker, G.P., 2008. Petrology of the 2004-2006 Mount St. Helens Lava Dome – Implications for Magmatic Plumbing and Eruption Triggering. https://doi.org/10.3133/pp175030.

Pistone, M., Caricchi, L., Ulmer, P., Burlini, L., Ardia, P., Reusser, E., Marone, F., Arbaret, L., 2012. Deformation experiments of bubble- and crystal-bearing magmas: rheological and microstructural analysis. J. Geophys. Res. Solid Earth 117. https://doi.org/10.1029/2011JB008986.

Pistone, M., Cordonnier, B., Caricchi, L., Ulmer, P., Marone, F., 2015. The viscous to brittle transition in crystal- and bubble-bearing magmas. Front. Earth Sci. 3. https://www.frontiersin.org/articles/10.3389/feart.2015.00071.

Reubi, O., Blundy, J., Varley, N.R., 2013. Volatiles contents, degassing and crystallisation of intermediate magmas at Volcan de Colima, Mexico, inferred from melt inclusions. Contrib. Mineral. Petrol. 165, 1087–1106. https://doi.org/10.1007/s00410-013-0849-6.

Rose, W.I., 1973. Nuée ardente from santiaguito volcano April 1973. Bull. Volcanol. 37, 365–371. https://doi.org/10.1007/BF02597634.

Sahetapy-Engel, S.T.M., Flynn, L.P., Harris, A.J.L., Bluth, G.J., Rose, W.I., Matias, O., 2004. Surface temperature and spectral measurements at Santiaguito lava dome, Guatemala. Geophys. Res. Lett. 31. https://doi.org/10.1029/2004GL020683.

Sammis, C.G., Ashby, M.F., 1986. The failure of brittle porous solids under compressive stress states. Acta Metall. 34, 511–526.

Scott, J.A.J., Mather, T.A., Pyle, D.M., Rose, W.I., Chigna, G., 2012. The magmatic plumbing system beneath Santiaguito Volcano, Guatemala. J. Volcanol. Geotherm. Res. 237–238, 54–68. https://doi.org/10.1016/j.jvolgeores.2012.05.014.

Sherrod, D.R., Scott, W.E., Stauffer, P.H., 2008. A Volcano Rekindled: The Renewed Eruption of Mount St. Helens, 2004-2006. https://doi.org/10.3133/pp1750.

Smith, R., Sammonds, P.R., Tuffen, H., Meredith, P.G., 2011. Evolution of the mechanics of the 2004–2008 Mt. St. Helens lava dome with time and temperature. Earth Planet. Sci. Lett. 307, 191–200. https://doi.org/10.1016/j.epsl.2011.04.044.

Sparks, R.S.J., 1997. Causes and consequences of pressurisation in lava dome eruptions. Earth Planet. Sci. Lett. 150, 177–189. https://doi.org/10.1016/S0012-821X(97)00109-X.

Stix, J., Torres, R.C., Narváez, M.L., Cortés, J.G.P., Raigosa, J.A., Gómez, M.D., Castonguay, R., 1997. A model of vulcanian eruptions at Galeras volcano, Colombia. J. Volcanol. Geotherm. Res. 77, 285–303. https://doi.org/10.1016/S0377-0273(96)00100-X.

Thomas, M.E., Neuberg, J., 2012. What makes a volcano tick—a first explanation of deep multiple seismic sources in ascending magma. Geology 40, 351–354. https://doi.org/10.1130/G32868.1.

Truby, J.M., Mueller, S.P., Llewellin, E.W., Mader, H.M., 2015. The rheology of three-phase suspensions at low bubble capillary number. Proc. Roy. Soc. A Math. Phys. Eng. Sci. 471. https://doi.org/10.1098/rspa.2014.0557.

Tuffen, H., Smith, R., Sammonds, P.R., 2008. Evidence for seismogenic fracture of silicic magma. Nature 453, 511–514. https://doi.org/10.1038/nature06989.

Vairé, E., Heap, M.J., Baud, P., van Wyk de Vries, B., 2024. Quantifying the physical and mechanical heterogeneity of porous volcanic rocks from the Chaîne des Puys (Massif

Central, France). Bull. Volcanol. 86, 49. https://doi.org/10.1007/s00445-024-01742-8.

Varley, N.R., Connor, C.B., Komorowski, J.C., 2019. Volcan de Colima. Portrait of a persistently active volcano. Springer Verlag, Berlin, p. 312.

Vasseur, J., Wadsworth, F.B., Heap, M.J., Main, I.G., Lavallée, Y., Dingwell, D.B., 2017. Does an inter-flaw length control the accuracy of rupture forecasting in geological materials? Earth and Planet. Sci. Lett. 475, 181–189.

Vasseur, J., Wadsworth, F.B., Dingwell, D.B., 2018. Forecasting multiphase magma failure at the laboratory scale using acoustic emission data. Front. Earth Sci. 6, 132. https://doi.org/10.3389/feart.2018.00132.

Vasseur, J., Wadsworth, F.B., Dingwell, D.B., 2023. Shear thinning and brittle failure in crystal-bearing magmas arise from local non-Newtonian effects in the melt. Earth Planet. Sci. Lett. 603, 117988. https://doi.org/10.1016/j.epsl.2023.117988.

Vasseur, J., Wadsworth, F.B., Dingwell, D.B., Lavallée, Y., 2024. Plug flow and brecciation in volcanic conduits can emerge from shear-induced crystal migration in otherwise Newtonian magmas. Commun. Earth Environ. 5, 389. https://doi.org/10.1038/s43247-024-01556-8.

Voight, B., Elsworth, D., 2000. Instability and collapse of hazardous gas-pressurized lava domes. Geophys. Res. Lett. 27, 1–4. https://doi.org/10.1029/1999GL008389.

Wadsworth, F.B., Witcher, T., Vossen, C.E.J., Hess, K.U., Unwin, H.E., Scheu, B., Castro, J.M., Dingwell, D.B., 2018. Combined effusive-explosive silicic volcanism straddles the multiphase viscous-to-brittle transition. Nat. Commun. 9, 1–8. https://doi.org/10.1038/s41467-018-07187-w.

Wallace, P.A., et al., 2019. Petrological architecture of a magmatic shear zone: a multidisciplinary investigation of strain localisation during magma ascent at Unzen Volcano, Japan. J. Petrol. 60, 791–826. https://doi.org/10.1093/petrology/egz016.

Walter, T.R., Harnett, C.E., Varley, N., Bracamontes, D.V., Salzer, J., Zorn, E.U., Bretón, M., Arámbula, R., Thomas, M.E., 2019. Imaging the 2013 explosive crater excavation and new dome formation at Volcán de Colima with TerraSAR-X, time-lapse cameras and modelling. J. Volcanol. Geotherm. Res. 369, 224–237. https://doi.org/10.1016/j.jvolgeores.2018.11.016.

Watts, R.B., Herd, R.A., Sparks, R.S.J., Young, S.R., 2002. Growth patterns and emplacement of the andesitic lava dome at Soufrière Hills Volcano, Montserrat. In: Druitt, T.H., Kokelaar, B.P. (Eds.), The Eruption of Soufrière Hills Volcano, Montserrat from 1995 to 1999, vol. 21. https://doi.org/10.1144/GSL.MEM.2002.021.01.06, p. 0.

Webb, S.L., Dingwell, D.B., 1990. Non-Newtonian rheology of igneous melts at high stresses and strain rates: experimental results for rhyolite, andesite, basalt, and nephelinite. J. Geophys. Res. 95, 15695–15701.

Wong, T., David, C., Zhu, W., 1997. The transition from brittle faulting to cataclastic flow in porous sandstones: mechanical deformation. J. Geophys. Res. Solid Earth 102, 3009–3025. https://doi.org/10.1029/96JB03281.

Zorn, E.U., Le Corvec, N., Varley, N.R., Salzer, J.T., Walter, T.R., Navarro-Ochoa, C., Vargas-Bracamontes, D.M., Thiele, S.T., Arámbula Mendoza, R., 2019. Load stress Controls on Directional Lava Dome Growth at Volcán de Colima, Mexico. Front. Earth Sci. 7, 84. https://www.frontiersin.org/article/10.3389/feart.2019.00084.

Zorn, E.U., Walter, T.R., Johnson, J.B., Mania, R., 2020. UAS-based tracking of the Santiaguito Lava Dome, Guatemala. Sci. Rep. 10, 8644. https://doi.org/10.1038/s41598-020-65386-2.